Supplemental Material for "Fano-like resonance due to interference with distant transitions"

Y.-N. Lv (吕亚男),[1,2,*] A.-W. Liu (刘安雯),[2,3,*] Y. Tan (谈艳),[2,3,*] C.-L. Hu (胡常乐),[3] T.-P. Hua (华天鹏),[3] X.-B. Zou (邹旭波),[1,2] Y. R. Sun (孙羽),[2,3,5,†] C.-L. Zou (邹长铃),[1,2,4,‡] G.-C. Guo (郭光灿),[1,2] and S.-M. Hu (胡水明)[2,3,§]

[1] *CAS Key Laboratory of Quantum Information, University of Science and Technology of China, Hefei, Anhui 230026, P. R. China*
[2] *Hefei National Laboratory, University of Science and Technology of China, Hefei 230088, China*
[3] *Department of Chemical Physics, University of Science and Technology of China, Hefei 230026, China*
[4] *State Key Laboratory of Quantum Optics and Quantum Optics Devices, and Institute of Opto-Electronics, Shanxi University, Taiyuan 030006, China*
[5] *Institute of Advanced Science Facilities, Shenzhen, 518107, China*

* These authors contributed equally to this work.
† robert@ustc.edu.cn
‡ clzou321@ustc.edu.cn
§ smhu@ustc.edu.cn

CONTENTS

I. Experimental Methods S1

II. Analytical derivation S7
A. Hamiltonian of the full-system S7
B. Two-level limit ($\Omega_{23}(t) = 0$) S7
1. Absorption spectrum S9
2. Saturated Absorption Spectrum (SAS) S9
C. Three-level model ($\Omega_{23}(t) \neq 0$) S12
1. Condition that two-level approximation is not valid S12
2. Effective two-level model and the Hamiltonian S13
D. Principle of the proposed nonlinear Fano-like resonance S13
E. Analytic derivation of asymmetric spectral profile S15
1. Doppler-free Lamb-dip spectrum S15
2. Estimation of the Fano factor S17
F. Theoretical discussion of the CO_2 experiments S17

III. Numerical calculation of the absorption spectrum S18
A. Method for Numerical calculation S18
B. Comparison of the analytic results of the Fano factor(q) with the numerical results S19
C. Simulation for hydrogen deuteride(HD) S20
D. Frequency shift due to NFR for CO_2 S22

References S23

I. EXPERIMENTAL METHODS

We picked CO_2 as the subject of our investigation and the infrared transitions of CO_2 in this range have been well documented in databases. The parameters and experimental conditions for all the experimental data presented in Fig. 4 in the Main Text are summarized in Supplemental Table I. The Doppler broadened absorption spectra of CO_2 near 6414 cm^{-1} simulated under the experimental conditions is shown in Supplemental Fig. 1. The detuning from the nearest transition to our target line is approximately 1.6 GHz, which is more than 3000 times the measured Lamb dip's width of 0.5 MHz. Note that all the ro-vibrational transitions of CO_2 in the infrared, including those "strong" lines, are actually far weaker than distant electronic transitions: Einstein A-coefficients for all these infrared transitions are well below 1 s^{-1} (weaker than strong electronic transitions by 8 orders of magnitude or even more). As a result, we excluded the possibility of asymmetry due to perturbations from nearby infrared transitions.

Saturated absorption spectroscopy measurements in this work were implemented with two independent setups with different methods: cavity ring-down spectroscopy (CRDS) and wavelength-modulated cavity-enhanced absorption spectroscopy (WM-CEAS). Details of the CRDS instrument are given in Supplemental Fig. 2. Two exemplary spectra of $^{13}C^{16}O_2$ lines at 6243.476 cm^{-1} and 6270.020 cm^{-1} are shown in Supplemental Fig. 3, showing symmetric and asymmetric lineshapes for two transitions with high and low Einstein A-coefficients, respectively. The configuration of the WM-CEAS instrument is described in Supplemental Fig. 4. Typical results of $^{12}C^{16}O_2$ lines recorded by the WM-CEAS method are shown in Supplemental Fig. 5.

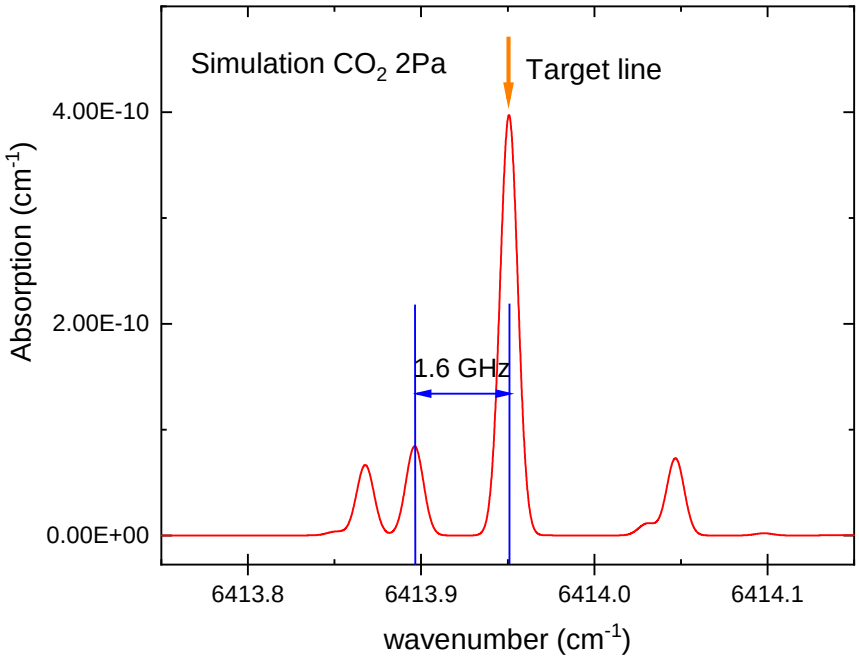

Supplemental Figure 1. Doppler broadened absorption spectrum of CO_2 under the experimental conditions simulated with the line list given in the HITRAN database.

Supplemental Table I. The parameters and Fano factors for experimental results of different transitions observed in this work.

Molecule	Line parameters[a]			Power[b]	q[c]
	Position(cm^{-1})	Intensity (cm/molecule)	A (s^{-1})	(W)	
$^{13}CO_2$	6270.0204	5.64E-26	2.31E-5	140	0.383(54)
	6271.5180	6.67E-26	2.80E-5	140	0.374(03)
	6273.0087	7.51E-26	3.31E-5	140	0.187(19)
	6274.4927	8.09E-26	3.84E-5	140	0.175(25)
	6243.5668	1.09E-25	7.25E-3	140	-0.010(5)
	6243.5436	6.03E-26	2.42E-3	140	0.058(11)
	6243.5381	4.17E-26	1.21E-3	140	0.003(12)
	6243.4758	3.17E-26	7.26E-4	140	0.030(18)
	6243.4863	2.53E-26	4.83E-4	140	0.030(18)
	6253.8955	2.01E-23	8.17E-3	90	0.008(3)
				40	-0.002(2)
				15	0.001(1)
				5	0.003(1)
$^{12}CO_2$	6413.9526	1.03E-26	1.03E-5	805	0.343(15)
				1570	0.434(15)
	6479.5776	1.08E-24	8.42E-4	1030	-0.011(4)

[a] Line positions and intensities as well as the Einstein A-coefficients A were taken from the HITRAN database [1].
[b] Laser power inside the high-finesse cavity.
[c] Fano coefficient derived from fitting the spectra.

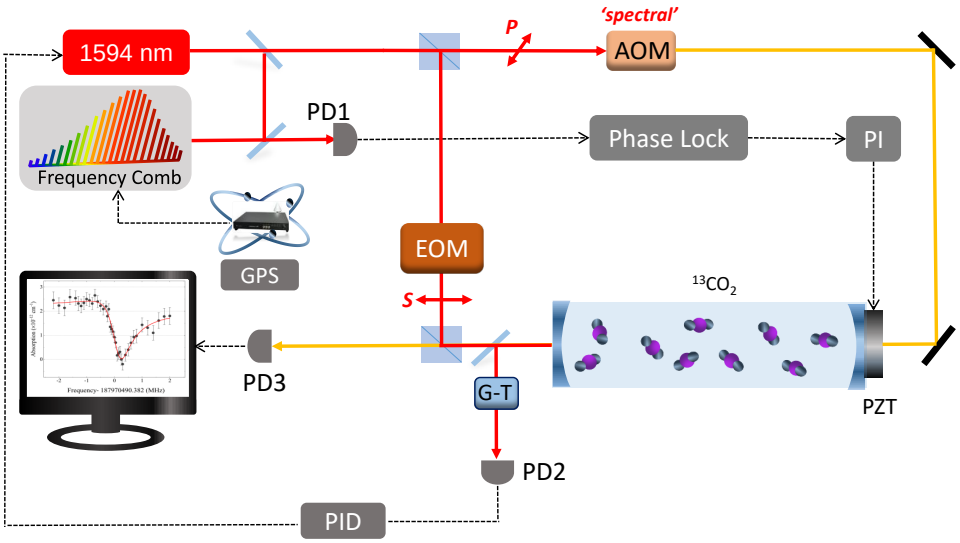

Supplemental Figure 2. Schematic configuration of the experimental setup for cavity ring-down spectroscopy (CRDS). Abbreviations: AOM: acousto-optical modulator, PD: photodiode detector, PI: proportion integration amplifier, PZT: piezoelectric actuator, G-T: Glan-Taylor prism. A 1594 nm external-cavity diode laser (Toptica CTL-1550) was locked to a temperature-stabilized high-finesse cavity (HFC) using the PDH method. The HFC is composed of a pair of high-reflectivity mirrors ($R \approx 0.99995$ in 1.54 - 1.7 μm) separated by a distance of 108.0 cm. The HFC length was stabilized through a PZT driven by a phase-lock circuit based on the beat signal between the laser and an optical frequency comb. The comb was referenced to a GPS-disciplined rubidium clock (GPS Reference-2000) with a stated relative frequency stability of 1×10^{-11} at 1 s. Part of the probe laser beam passed an AOM and then coupled into the cavity. The AOM was driven by a radio frequency (RF) source and the frequency was set exactly equal to the free-spectral-range of the HFC (138.86 MHz). A rectangular wave of 500 Hz was applied on the RF source, which repeatedly produced ring-down events. The decay time τ, which relates to the cavity loss including the absorption of the sample gas, was retrieved by fitting the ring-down signal with an exponential decay function.

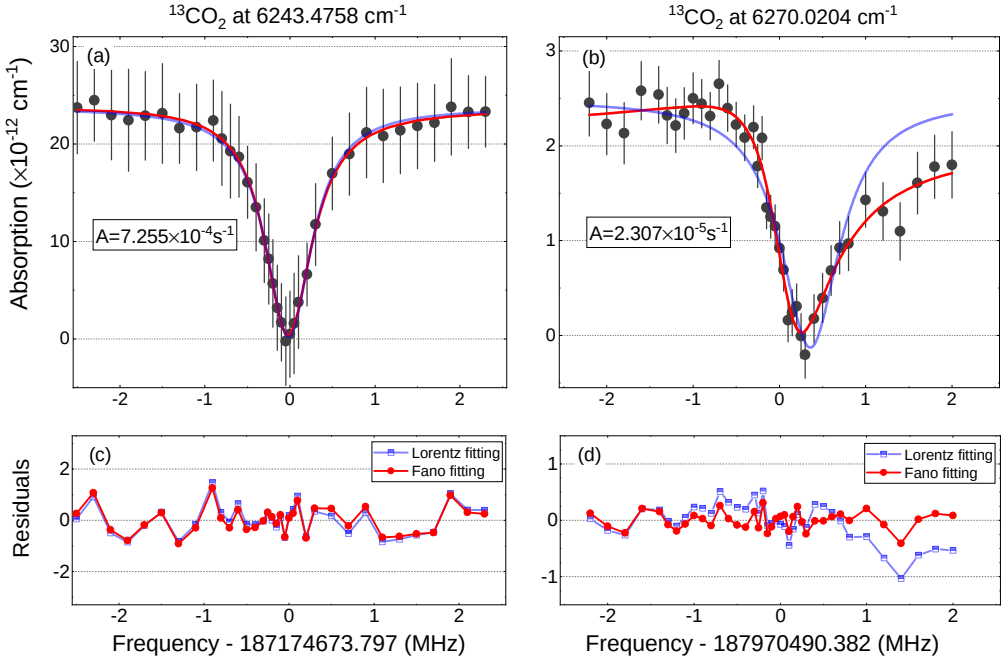

Supplemental Figure 3. The recorded spectra of two ro-vibrational transitions of $^{13}C^{16}O_2$ by cavity ring-down spectroscopy (CRDS). ^{13}C-enriched carbon dioxide sample with stated $^{13}CO_2$ abundance >99% was used, with a sample gas pressure of 2 Pa at room temperature. (a) The Q(4) line in the 31112 - 01101 band at 6243.4758 cm^{-1} with an Einstein A-coefficient of 7.26×10^{-4} s^{-1}. (b) The R(16) line in the 41101 - 00001 band at 6270.0204 cm^{-1} with an Einstein A-coefficient of 2.31×10^{-5} s^{-1}. Scattered points are experimental data. Blue and red lines are fitting results by Lorentzian and Fano profiles, respectively. The fitting residuals are shown in the lower panels (c) and (d).

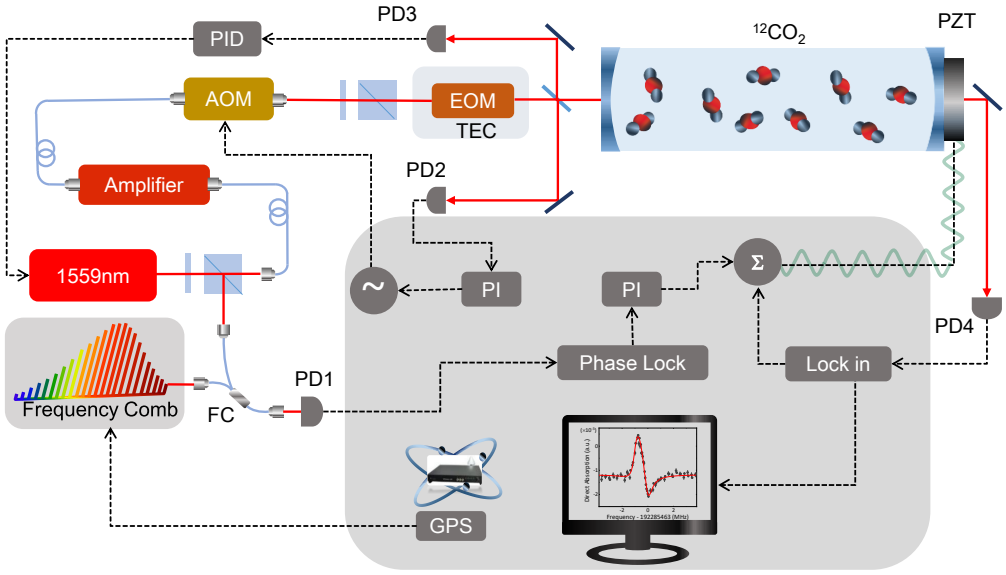

Supplemental Figure 4. Configuration of the experimental setup for wavelength-modulated cavity-enhanced absorption spectroscopy (WM-CEAS). Abbreviations: AOM: acousto-optical modulator; EOM: electro-optical modulator; FC: fiber coupler; TEC: temperature-controller; PD: photodiode detector; PI: proportion integration amplifier; PZT: piezoelectric actuator; PC: personal computer. An 1559 nm external-cavity diode laser (Toptica DL Pro), amplified by a fiber-amplifier (Koheras Boostik HPA), was locked to a longitudinal mode of a 44.6 cm HFC by the Pound-Drever-Hall method. A TEC unit was used to stabilize the temperature of the EOM to reduce the residual amplitude modulation. A phase-lock circuit (after PD1) was used to lock the beat frequency between the laser and an optical frequency comb. It was the same comb used in the CRDS measurement. A photodetector (PD2) was used to monitor the laser power before the HFC and the signal was sent to a locking servo to stabilize the laser power by changing the driving signal applied on the AOM. A direct CEAS scan could be implemented by tuning the beat frequency, and the $1f$-demodulated WM-CEAS signal (after PD4) was obtained when a dither signal from a lock-in amplifier (SRS 830) was applied on the PZT attached to one of the high-reflective mirrors.

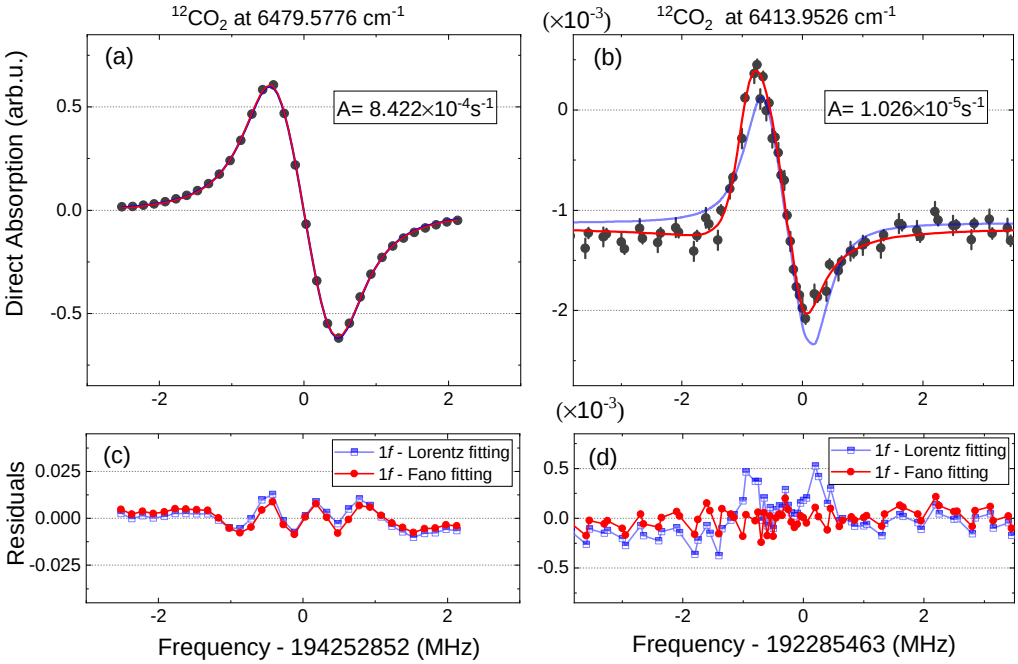

Supplemental Figure 5. Typical experimental spectra for two ro-vibrational transitions of the $^{12}C^{16}O_2$ molecule by wavelength-modulated cavity-enhanced absorption spectroscopy (WM-CEAS). Spectra were recorded at room temperature (296 K) and a sample gas pressure of 2 Pa. (a) The WM-CEAS spectrum of the relatively strong transition, P(28) in the (30011) ← (00001) band, at 6479.5776 cm^{-1} which has an Einstein A-coefficient of 8.42×10^{-4} s^{-1}. (b) The WM-CEAS spectrum of the relatively weak transition, R(32) in the (41101) ← (00001) band, at 6413.9526 cm^{-1} with an Einstein A-coefficient of 1.03×10^{-5} s^{-1}. The same dither signal and demodulation circuit were applied in the measurements of both lines. Scattered points are experimental data. Blue and red lines are the fitting results with derivative Lorentzian and derivative Fano profiles, respectively. The fitting residuals are shown in the lower panels (c) and (d).

II. ANALYTICAL DERIVATION

In this section, we provide detailed derivations supporting the discussions presented in the main text. All the symbols involved in this study are summarized in Table II and their corresponding definitions are provided as well. In the following section, detailed derivations of the two-level and three-level molecules that interact with the probe light are presented. The essential details for the analytical derivation of the asymmetric Doppler-free absorption spectrum are derived under the approximation of two lowest-order sidebands due to the AC Stark shift modulation. Additionally, the numerical methods to calculate the system absorption spectrum with the full model are stated in Sec.(III), where more numerical results are presented.

A. Hamiltonian of the full-system

For the model considered in our theoretical studies, N three-level molecules (or atoms) are coupled to a standing-wave probe light field, as shown in Fig. 1(a) in the main text. The system Hamiltonian considering the Doppler effect reads ($\hbar$=1)

$$H = \sum_j H_j, \tag{1}$$

with

$$H_j = \omega_{12}\sigma_{22}^j + \omega_{13}\sigma_{33}^j + \left(\frac{\Omega_{12,j}(t)}{2}e^{i\omega_p t}\sigma_{12}^j + \frac{\Omega_{23,j}(t)}{2}e^{i\omega_p t}\sigma_{23}^j + h.c.\right) \tag{2}$$

describing the j-th molecule. Here, $h.c.$ denotes the Hermitian conjugate, σ_{ab} corresponds to the jumping operator $|a\rangle\langle b|$ between energy levels $|a\rangle$ and $|b\rangle$, and ω_{ab} is the frequency difference between them. The molecule-light coupling is given by the Rabi frequency

$$\Omega_{ab,j}(t) = 2d_{ab} \times \xi \times 2\cos[k_p(v_j t + z_{j,0})]. \tag{3}$$

Here, d_{ab} is the electric dipole moment between energy levels $|a\rangle$ and $|b\rangle$, ξ is the standing-wave amplitude, k_p is the wavevector of the probe field, $z_{j,0}$ is the initial location of the molecule in the axial direction, and v_j is the velocity for the j-th molecule along the direction of the probe laser beam. For the j-th molecule, in the rotating frame of $\omega_p\sigma_{22}^j + 2\omega_p\sigma_{33}^j$, the Hamiltonian can be simplified to

$$H_j = -\Delta_{12}\sigma_{22}^j - \Delta_{23}\sigma_{33}^j + \left(\frac{\Omega_{12,j}(t)}{2}\sigma_{12}^j + \frac{\Omega_{23,j}(t)}{2}\sigma_{23}^j + h.c.\right), \tag{4}$$

where $\Delta_{12} = \omega_p - \omega_{12}$ and $\Delta_{23} = 2\omega_p - \omega_{13}$ are the detunings of the transitions with respect to the probe laser. For a single molecule, its quantum state can be described by a density matrix ρ, and the evolution of its density matrix $\rho_{ab}(|a\rangle\langle b|)$ follows the Master equation [2]:

$$\frac{\mathrm{d}\rho}{\mathrm{d}t} = -i[H,\rho] + \sum_i \gamma_i(L_i\rho L_i^\dagger - \frac{1}{2}L_i^\dagger L_i\rho - \frac{1}{2}\rho L_i^\dagger L_i) \tag{5}$$

where L_i is a dissipative jump operator and γ_i is the corresponding decoherence rate. In this work, we consider the spontaneous emission of the energy levels, thus $L_i \in [\sigma_{12}, \sigma_{13}, \sigma_{23}]$.

B. Two-level limit ($\Omega_{23}(t) = 0$)

In most experiments, the probe laser is always near-resonant with the target transition. Although there are many transitions in the molecule, other excess transitions have detunings that are orders of magnitude larger than the interaction strengths in the system and hence are neglected in practicality. For instance, for excess energy level $|3\rangle$, we have $|\omega_p - \omega_{23}| \gg \Omega_{12}, \Omega_{23}$, thus the far-off resonance transition is greatly suppressed. For simplicity, this transition is ignored in conventional studies of light-matter interactions by setting $\Omega_{23}(t) = 0$. Then, we can approximate the

Supplemental Table II. Table of all symbols presented in this work.

Symbol	**Description**	**Remark**
ω_p	frequency of the probe field	
ω_{ab}	transition frequency between two levels $\|a\rangle$ and $\|b\rangle$	
γ_{ab}	decay rate from $\|b\rangle$ to $\|a\rangle$	
$\mathcal{P}$	excitation probability to energy level $\|2\rangle$	
I	intensity of probe field	
τ	transit time	
Δ_B	transit-time broadening	$\Delta_B = 1/\tau$
Δ_{ab}	detuning between the probe field and the transition from $\|a\rangle$ to $\|b\rangle$	$\Delta_{ab} = \omega_p - \omega_{ab}$
Ω_{ab}	Rabi frequency of transition from $\|a\rangle$ to $\|b\rangle$ probing by the probe field	
γ_3	decay rate of energy level $\|3\rangle$	
δ	modulation amplitude on energy level $\|2\rangle$	
k_p	wave vector of the probe field	
j	noting the j-th molecule	
v_j	longitudinal velocity for the j-th molecule	
v_t	transverse velocity	
c	speed of light	
ϵ_0	permittivity of vacuum	
$\hbar$	Planck's constant	
z_j	instant location of the j-th molecule	$z_j = v_j t + z_{j,0}$
$z_{j,0}$	initial location of the j-th molecule	
ζ_j	variate of Bessel function, related to δ, k_p ang v_j	$\zeta_j = \delta/4k_p v_j$
$J_{\pm n}(\zeta_j)$	Bessel function of order n and variate ζ_j	
q	Fano factor	
ω_s	frequency shift of the Fano profile from fitting	
Γ	linewidth of the Fano profile from fitting	
A, B	fitting parameters of the Fano function	
H	Hamiltonian	
ρ_{ab}	density matrix element	
σ_{ab}	transition operator from $\|b\rangle$ to $\|a\rangle$ i.e. $\|a\rangle\langle b\|$	
d_{ab}	dipole moment of transition from $\|a\rangle$ to $\|b\rangle$	
$\langle v\rangle$	ensemble average of the longitudinal velocity v_j	
$\langle\tau\rangle$	ensemble average of transit time τ	
m	mass of the molecule	
k_B	Boltzmann constant	
r	beam waist width of the standing-wave field	
ξ	amplitude of the standing-wave field	

molecule with many transitions to a two-level model, and the corresponding Hamiltonian becomes

$$H_j = -\Delta_{12}\sigma_{22}^j + \left(\frac{\Omega_{12,j}(t)}{2}\sigma_{12}^j + h.c.\right). \tag{6}$$

1. Absorption spectrum

In optical spectroscopy, the absorption line is acquired by measuring the transmission of the probe laser or the induced fluorescence by scanning the laser frequency. Theoretically, we should solve the dynamics of the density matrix element $\rho(t)$ to produce the absorption spectrum. For an ensemble, the real and imaginary parts of the susceptibility are contributed by the real and imaginary parts of the nondiagonal density matrix elements, which correspond to the dispersion and absorption of the medium respectively. Based on the Hamiltonian Eq. (6) and the master equation Eq. (5), the evolution of the system follows

$$\frac{\mathrm{d}\rho_{12}^{j}(t)}{\mathrm{d}t} = \left(-i\Delta_{12} - \frac{\gamma_{12}}{2}\right)\rho_{12}^{j} + i\frac{\Omega_{12,j}(t)^{*}}{2}(\rho_{11}^{j} - \rho_{22}^{j}). \tag{7}$$

Here, γ_{12} is the spontaneous emission rate from $|2\rangle$ to $|1\rangle$. Considering that the molecular gas is at room-temperature and energy level $|2\rangle$ is long-lived state, we can make an approximation $\rho_{22} \simeq 0$, $\rho_{11} \simeq 1$. With this approximation, the saturation effect of the two-level system is removed, and then we can resolve the system absorption spectrum to the linear limit.

Therefore, we obtain $\rho_{12}(t)$ based on the initial condition $\rho_{12}(0) = 0$ as

$$\begin{aligned}\rho_{12}^{j}(t) \simeq & d_{12}\xi\left(\frac{e^{ikv_j t}}{kv - i\gamma_{12}/2 + \Delta_{12}} + \frac{e^{-ikv_j t}}{-kv - i\gamma_{12}/2 + \Delta_{12}}\right) + \\ & d_{12}\xi e^{\left(-i\Delta_{12} - \frac{\gamma_{12}}{2}\right)t}\left(\frac{-1}{kv - i\gamma_{12}/2 + \Delta_{12}} + \frac{-1}{-kv - i\gamma_{12}/2 + \Delta_{12}}\right).\end{aligned} \tag{8}$$

Obviously, the imaginary part of $\rho_{12}(t)$ is a function being symmetric with respect to the detuning (Δ_{12}) since it is the result of a sum over the Lorentz function. Thus a typical symmetric absorption spectrum is acquired in previous studies when ignoring the influence of far-off resonance coupling. Then, the probability of exciting the molecule to level $|2\rangle$ is calculated as

$$\mathcal{P} = \int_0^t \Omega_{12}^{*}(t')\mathrm{Im}\left[\rho_{12}(t')\right] dt'. \tag{9}$$

Here, the integration of time is counting from the uniform distribution of molecules in the standing-wave field. As a result, the absorption spectrum of the ensemble of the two-level system can be obtained by averaging over the ensemble of molecules, and a conventional symmetric spectral profile is expected. Notably, the saturation effect is excluded in Eq. (8) and Eq. (9), because we have assumed $\rho_{22} \simeq 0$, $\rho_{11} \simeq 1$ at first.

2. Saturated Absorption Spectrum (SAS)

In this section, we will recall the absorption spectrum without taking the linear approximation and the saturation effect is included. Considering that the spontaneous emission rate of $|2\rangle$ is very small, for the ultraweak transitions considered in this work, we can treat each molecule as a closed quantum system [2] because the spontaneous emission is negligible when the molecule passes through the probe laser beam. Then, we can solve the evolution of the states more conveniently in a closed system. As a consequence, the probability $\mathcal{P}$ of the probe field exciting the molecule to a long-lived energy level $|2\rangle$ is calculated based on the Hamiltonian and Schrodinger equation.

In the rotating-frame, Eq. (6) can also be written as

$$H_j = d_{12}\xi\left[e^{-i(-\Delta_{12} - k_p v_j)t + ik_p z_{j,0}} + e^{-i(-\Delta_{12} + k_p v_j)t - ik_p z_{j,0}}\right]\sigma_{12}^{j} + h.c. \tag{10}$$

Moreover, considering that the standing-wave field amplitude follows a Gaussian distribution in the direction perpendicular to the cavity-axis, when the j-th molecule passes through the standing-wave field, the coupling Rabi frequency follows a Gaussian distribution over time. Then, the Hamiltonian can be rewritten as

$$H_j = d_{12}\xi e^{-\frac{t^2}{2\tau^2}}[e^{-i(-\Delta_{12} - k_p v_j)t + ik_p z_{j,0}} + e^{-i(-\Delta_{12} + k_p v_j)t - ik_p z_{j,0}}]\sigma_{12}^{j} + h.c. \tag{11}$$

Here τ is the transit time, which is related to the beam waist width of the standing-wave field and transverse velocity

of molecules. We define the state of the j-th molecule as

$$|\psi_j(t)\rangle = a(t)|1\rangle + b(t)|2\rangle, \tag{12}$$

whose evolution follows the Schrodinger equation

$$i\hbar\frac{\partial|\psi_j(t)\rangle}{\partial t} = H_j|\psi_j(t)\rangle \tag{13}$$

Given the initial state $|1\rangle$, with the approximation that $d_{12}\xi\tau \ll 1$, the solution of $|\psi_j(t)\rangle$ could be represented as

$$|\psi_j(t)\rangle = \cos\left[\theta_j(t)\right]|1\rangle - i\sin\left[\theta_j(t)\right]|2\rangle, \tag{14}$$

with the interaction angle induced by the Rabi frequency of the probe field as

$$\begin{aligned}\theta_j(t) =& \int_{-\infty}^{\infty} d_{12}\xi e^{-\frac{t^2}{2\tau^2}}\left[e^{-i(-\Delta_{12}-k_p v_j)t+ik_p z_{j,0}} + e^{-i(-\Delta_{12}+k_p v_j)t-ik_p z_{j,0}}\right]\mathrm{d}t \\ =& d_{12}\xi\sqrt{2\pi}\tau\left[e^{-\frac{1}{2}(-\Delta_{12}-k_p v_j)^2\tau^2+ik_p z_{j,0}} + e^{-\frac{1}{2}(-\Delta_{12}+k_p v_j)^2\tau^2-ik_p z_{j,0}}\right].\end{aligned} \tag{15}$$

Thus the probability $\mathcal{P}_j$ of the probe field exciting the j-th molecule to long-lived energy level $|2\rangle$ is presented approximatively as

$$\mathcal{P}_j \approx \left|\sin^2\left[\theta_j(t)\right]\right| \approx |\theta_j^2(t)| - \frac{1}{3}|\theta_j^4(t)|. \tag{16}$$

In our proposed model, molecules follow the Maxwell-Boltzmann distribution $f(v_j)$ shown in Eq. (51), thus $\mathcal{P}$ should be the results of average over the longitudinal velocity v_j, i.e.

$$\mathcal{P} = \int_{-\infty}^{\infty}\mathrm{d}v_j f(v_j)\int_0^{2\pi/k_p}\frac{dz_{j,0}}{2\pi/k_p}\mathcal{P}_j. \tag{17}$$

By applying the relations for the averaging of the molecule's initial location

$$\int_0^{2\pi/k_p}\frac{dz_{j,0}}{2\pi/k_p}\times e^{2ik_p z_{j,0}} = 0, \tag{18}$$

$$\int_0^{2\pi/k_p}\frac{dz_{j,0}}{2\pi/k_p}\times 1 = 1, \tag{19}$$

to the second-order term

$$|\theta_j^2(t)| = \left(d_{12}\xi\sqrt{2\pi}\tau\right)^2\left(e^{-(\Delta_{12}-k_p v_j)^2\tau^2} + e^{-(\Delta_{12}+k_p v_j)^2\tau^2} + 2\mathrm{Re}[e^{-(\Delta_{12}^2+k_p^2 v_j^2)\tau^2+2ik_p z_{j,0}}]\right), \tag{20}$$

we can solve

$$\begin{aligned}&\int_{-\infty}^{\infty} dv_j f\left(v_j\right)\int_0^{2\pi/k_p}\frac{dz_{j,0}}{2\pi/k_p}\left|\theta_j^2\left(t\right)\right| \\ =& \left(d_{12}\xi\sqrt{2\pi}\tau\right)^2\int_{-\infty}^{\infty} dv_j f\left(v_j\right)\left(e^{-(\Delta_{12}-k_p v_j)^2\tau^2} + e^{-(\Delta_{12}+k_p v_j)^2\tau^2}\right).\end{aligned} \tag{21}$$

Considering that only the molecules with longitudinal velocity satisfying the relation $\Delta_{12} \pm k_p v_j \approx 0$ dominate the

contribution to the absorption spectrum, we make the approximate that

$$\begin{aligned}
&\int_{-\infty}^{\infty} dv_j f\left(v_j\right)\left(e^{-\left(\Delta_{12}-k_p v_j\right)^2\tau^2}+e^{-\left(\Delta_{12}+k_p v_j\right)^2\tau^2}\right) \\
&\approx f\left(v_j=0\right)\int_{-\infty}^{\infty} dv_j\left(e^{-\left(\Delta_{12}-k_p v_j\right)^2\tau^2}+e^{-\left(\Delta_{12}+k_p v_j\right)^2\tau^2}\right) \\
&=f\left(v_j=0\right)\frac{\sqrt{2\pi}}{k_p\tau},
\end{aligned} \tag{22}$$

and then we can obtain

$$\begin{aligned}
\int_{-\infty}^{\infty} dv_j f\left(v_j\right)\int_0^{2\pi/k_p}\frac{dz_{j,0}}{2\pi/k_p}\left|\theta_j^2\left(t\right)\right| &\approx\left(d_{12}\xi\sqrt{2\pi}\tau\right)^2\frac{2\sqrt{\pi}}{k_p\tau}f\left(v_j=0\right) \\
&=4\pi^{3/2}\frac{f\left(v_j=0\right)}{k_p}\left(d_{12}\xi\right)^2\tau.
\end{aligned} \tag{23}$$

Similarly, for the fourth-order term, we have

$$\begin{aligned}
&\int_{-\infty}^{\infty} dv_j f\left(v_j\right)\int_0^{2\pi/k_p}\frac{dz_{j,0}}{2\pi/k_p}\left(\left|\theta_j^4\left(t\right)\right|\right) \\
=&\left(d_{12}\xi\sqrt{2\pi}\tau\right)^4\int_{-\infty}^{\infty} dv_j f\left(v_j\right) \\
&\times\int_0^{2\pi/k_p}\frac{dz_{j,0}}{2\pi/k_p}\left(e^{-\left(\Delta_{12}-k_p v_j\right)^2\tau^2}+e^{-\left(\Delta_{12}+k_p v_j\right)^2\tau^2}+2\mathrm{Re}[e^{-\left(\Delta_{12}^2+k_p^2 v_j^2\right)\tau^2+2ik_p z_{j,0}}]\right)^2.
\end{aligned}$$

According to the relations in Eq. (19) and

$$\int_0^{2\pi/k_p}\frac{dz_{j,0}}{2\pi/k_p}\times\cos^2\left(2k_p z_{j,0}\right)=\frac{1}{2}, \tag{24}$$

we obtain

$$\begin{aligned}
&\int_{-\infty}^{\infty} dv_j f\left(v_j\right)\int_0^{2\pi/k_p}\frac{dz_{j,0}}{2\pi/k_p}\left(\left|\theta_j^4\left(t\right)\right|\right) \\
=&\left(d_{12}\xi\sqrt{2\pi}\tau\right)^4\int_{-\infty}^{\infty} dv_j f\left(v_j\right)\left\{e^{-2\left(\Delta_{12}-k_p v_j\right)^2\tau^2}+e^{-2\left(\Delta_{12}+k_p v_j\right)^2\tau^2}+4e^{-2\left(\Delta_{12}^2+k_p^2 v_j^2\right)\tau^2}\right\} \\
\approx&\left(d_{12}\xi\sqrt{2\pi}\tau\right)^4\frac{f\left(v_j=0\right)\sqrt{\frac{\pi}{2}}}{k_p\tau}\left(2+4e^{-2\Delta_{12}^2\tau^2}\right) \\
=&4\sqrt{2}\pi^{5/2}\frac{f\left(v_j=0\right)}{k_p}\left(d_{12}\xi\right)^4\tau^3\left(1+2e^{-2\Delta_{12}^2\tau^2}\right).
\end{aligned} \tag{25}$$

Therefore, we can solve the absorption spectrum around $v_j\approx 0$ as

$$\mathcal{P}\approx 4\pi^{3/2}\frac{f\left(v_j=0\right)}{k_p}\left(d_{12}\xi\right)^2\tau-\frac{4\sqrt{2}\pi^{5/2}}{3}\frac{f\left(v_j=0\right)}{k_p}\left(d_{12}\xi\right)^4\tau^3\left(1+2e^{-2\Delta_{12}^2\tau^2}\right). \tag{26}$$

Obviously, the saturation effect induces a reduction in the population on $|2\rangle$ when increasing the drive amplitude ξ. The first term corresponds to the linear absorption component in which the excitation probability is proportional to the power of the probe laser $I\propto\xi^2$, and the second term indicates the saturation effect which is proportional to I^2. In particular, there is an additional saturation when the probe detuning Δ_{12} is very small, which is the well known SAS that the molecules with velocity around $v_j\approx 0$ experience a stronger drive amplitude of the standing wave and thus the saturation effect is more significant. Therefore, we obtain a symmetric Gaussian-like SAS profile around the center $\Delta_{12}\approx 0$ for two-level systems by ignoring the influence of far-off resonance coupling.

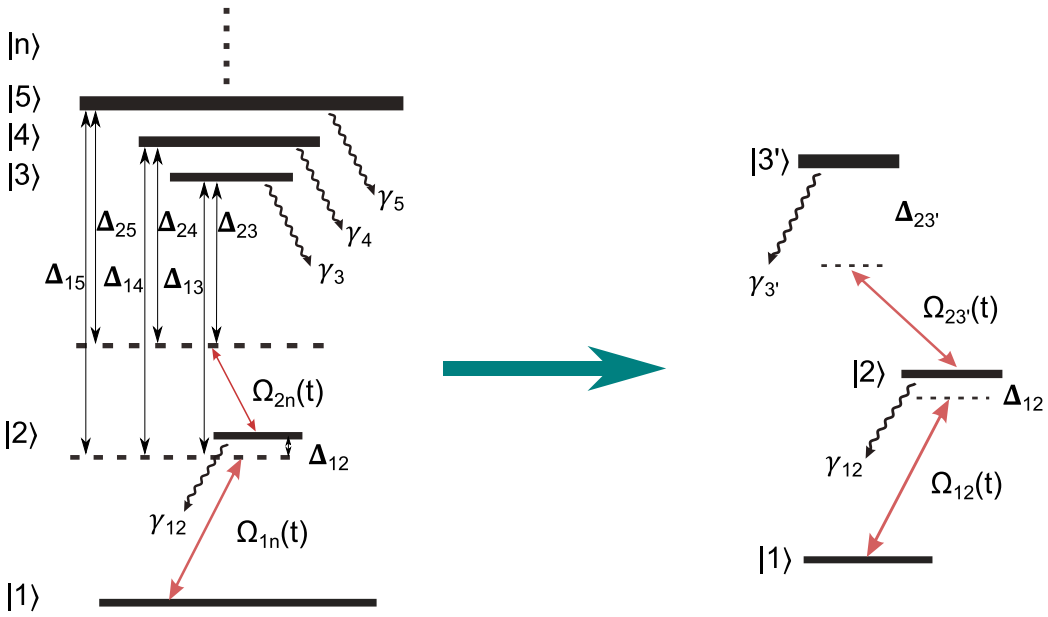

Supplemental Figure 6. Energy level structure of the full system with more than one excess far-off resonance coupling levels noted as $|n\rangle$ shown on the left and energy level structure of the equivalent model with only one excess far-off resonance coupling levels noted as $|3'\rangle$ on the right. The equivalent far-off resonance coupling level $|3'\rangle$ can induce the same AC Stark shift on $|2\rangle$ as the all levels $\sum_n|n\rangle$.

C. Three-level model ($\Omega_{23}(t) \neq 0$)

1. *Condition that two-level approximation is not valid*

For a long-lived two-level molecule interacting with a standing-wave field of amplitude ξ, the population on the long-lived energy level $|2\rangle$ is proportional to $\mathcal{P} \propto d^2\xi^2\tau^2$, where d_{12} is the electric dipole moment between $|1\rangle$ and $|2\rangle$. τ is the transit time, which depends on the beam waist width of the probe light and transverse velocity of the molecule. Considering $d_{12}^2 \propto \gamma_{12}$, $\xi^2 \propto I$ and $\tau = 1/\Delta_B$, we can obtain $\mathcal{P} \propto I\gamma_{12}/\Delta_B^2$, where I is the intensity of the optical field. To observe the Doppler-free absorption spectrum, the condition $\mathcal{P} \sim \mathcal{O}(10^{-4})$ should be satisfied. Although the narrow-linewidth transition ($|1\rangle \rightarrow |2\rangle$) is near-resonant, other excess transitions inevitably exist (as shown in Supplemental Fig. 6). For simplicity, we consider only one additional far-off resonance excited state $|3\rangle$ and the Rabi frequency of coupling with the probe field is $\Omega_{23} \propto \sqrt{I\gamma_{23}}$, where γ_{23} is the decay rate from $|3\rangle$ to $|2\rangle$. For the detuning between the probe light and the excess transition $|\Delta_{23}| = |\omega_p - \omega_{23}| \gg \Omega_{23}, \gamma_{23}$, we could neglect the population on $|3\rangle$ ($\sim \Omega_{23}^2/\Delta_{23}^2$) but keep the energy shift on $|2\rangle$ due to the AC Stark effect ($\delta \sim \Omega_{23}^2/\Delta_{23}$). Then we could estimate the modulation on frequency of $|2\rangle$ approximately as

$$\delta \propto \frac{\gamma_{23}}{\gamma_{12}}\mathcal{P}\frac{\Delta_B^2}{\Delta_{23}} \tag{27}$$

When the transit-time broadening $\Delta_B \gg \gamma_{12}$, the excessive effects can't be ignored ever if $|\delta|/\Delta_B$ is not negligible. If $\mathcal{P} \simeq 10^{-4}$, $\Delta_B/2\pi \simeq 10^6$ Hz, $\Delta_{23}/2\pi \simeq -10^{15}$ Hz, $\gamma_{23}/2\pi \simeq 10^8$ Hz, when $\gamma_{12}/2\pi < 10^{-4}$ Hz, the amplitude of AC Stark shift is comparable to the transit-time broadening, thus the far-off resonance coupling can't be ignored.

In fact, there may be more than one excess far-off resonance level such as $|n\rangle, (n = 3, 4, 5, ...)$ as shown in the left of Supplemental Fig. 6. The AC Stark shift is contributed by all excess far-off resonance transitions noted as σ_{1n} and σ_{2n}. Thus the total energy shift on $|2\rangle$ is $\sum_n'[(\mathrm{d_{2n}}\cdot\xi\cos(kv_jt))^2/\Delta_{2n} - (\mathrm{d_{1n}}\cdot\xi\cos(kv_jt))^2/\Delta_{1n}]$, where d_{2n} (d_{1n}) is the electric dipole moment between energy levels $|2\rangle$ ($|1\rangle$) and $|n\rangle$. ξ is the standing-wave amplitude. $\Delta_{2n} = \omega_p - \omega_{2n}$, $\Delta_{1n} = \omega_p - \omega_{1n}$. To simplify, an equivalent far-off resonance coupling level $|3'\rangle$ is proposed, which can induce the

same AC Stark shift amplitude, i.e.:

$$\delta \simeq \sum_n [\frac{(\mathrm{d}_{2n}\cdot\xi)^2}{\Delta_{2n}} - \frac{(\mathrm{d}_{1n}\cdot\xi)^2}{\Delta_{1n}}] = \frac{(\mathrm{d}_{23'}\cdot\xi)^2}{\Delta_{23'}} - \frac{(\mathrm{d}_{13'}\cdot\xi)^2}{\Delta_{13'}} \tag{28}$$

as shown on the right of Supplemental Fig. 6. Especially in the carbon dioxide system, the levels from a series states $^1\Pi_u$ (104 $\sim$ 110 nm) and $^1\Sigma_u^+$ (110 $\sim$ 114 nm) could possibly be involved in the far-off resonance coupling, according to the VUV absorption spectrum of CO_2 [3] and state-to-state photodissociation dynamics studies [4–6]. The full system with many excess far-off resonance transitions can also be simplified as a two-level model based on the large detuning condition. The influence from all excess far-off resonance energy levels is shown as an effective periodic energy shift on $|2\rangle$, as shown in Fig. 1b in the main text.

2. Effective two-level model and the Hamiltonian

When the far-off resonance coupling between σ_{23}^j and the standing-wave can not be ignored, the three-level model is acquired, as shown in Fig. 1b of the main text. Considering $|\Delta_{23}| \gg \Omega_{23,j}(t)$, we apply the fast-varying approximation that $\rho_{13}, \rho_{31}, \rho_{23}, \rho_{32}$ can arrive to the steady-state immediately, i.e. $\mathrm{d}\rho_{13}/\mathrm{d}t = 0$, $\mathrm{d}\rho_{31}/\mathrm{d}t = 0$, $\mathrm{d}\rho_{23}/\mathrm{d}t = 0$, $\mathrm{d}\rho_{32}/\mathrm{d}t = 0$. Substituting the steady-state solution of $\rho_{13}, \rho_{31}, \rho_{23}, \rho_{32}$ into the time dependent evolutionary differential equations of $\rho_{11}, \rho_{12}, \rho_{21}, \rho_{22}$, and considering γ_{12}, γ_{13}, $\Omega_{12,j}(t)$, $\Omega_{23,j}(t)$, $|\Delta_{12,j}| \ll |\Delta_{23,j}|$, we can obtain the simplified equation

$$\frac{\mathrm{d}\mathbf{Q}}{\mathrm{d}t} = \mathbf{M}\cdot\mathbf{Q} + \mathbf{a} \tag{29}$$

Here $\mathbf{Q} = \{\rho_{11}, \rho_{12}, \rho_{21}, \rho_{22}\}^T$, $\mathbf{a}$ is a constant vector for $\mathbf{a} = \{a_1, a_2, a_3, a_4\}^T$ and $\mathbf{M}$ is a coefficient matrix:

$$\mathbf{M} \simeq \begin{pmatrix} -\gamma_{13} & \frac{i\Omega_{12}(t)}{2} & \frac{-i\Omega_{12}(t)}{2} & -\gamma_{13}+\gamma_{12} \\ \frac{i\Omega_{12}(t)}{2} & -\frac{\gamma_{12}}{2} - i[\Delta_{12} - \frac{\delta}{2}(1+\cos(2kv_jt))] & 0 & \frac{-i\Omega_{12}(t)}{2} \\ \frac{-i\Omega_{12}^*(t)}{2} & 0 & -\frac{\gamma_{12}}{2} + i[\Delta_{12} - \frac{\delta}{2}(1+\cos(2kv_jt))] & \frac{i\Omega_{12}(t)}{2} \\ 0 & \frac{-i\Omega_{12}^*(t)}{2} & \frac{i\Omega_{12}^*(t)}{2} & -\gamma_{12}-\gamma_{23} \end{pmatrix} \tag{30}$$

where $\delta \times (\frac{1}{2} + \frac{1}{2}\cos(2kv_jt)) = \frac{\Omega_{23,j}^2(t)}{4\Delta_{23}}$ is the AC Stark shift on $|2\rangle$ from the excess far-off resonance transition $|2\rangle \to |3\rangle$, which is ignored in the two-level limit system because of $\Omega_{23}(t) \simeq 0$. Then an effective two-level model is acquired based on the large detuning condition and the influence of excess far-off resonance shown as the energy shift on $|2\rangle$ due to the AC Stark effect.

For the periodically modulated two-level scheme interacting with a standing-wave field, the effective Hamiltonian of the j-th molecule can be given by

$$H_j = \left[-\Delta_{12} + \frac{\delta}{2}(1+\cos(2kv_jt))\right]\sigma_{22}^j + \left[\frac{\Omega_{12,j}(t)}{2}\sigma_{12}^j + h.c.\right]. \tag{31}$$

D. Principle of the proposed nonlinear Fano-like resonance

Next, we briefly explain the principle of the proposed nonlinear Fano-like resonance and the reason for the asymmetrical absorption line-shape based on the Hamiltonian of the modulated two-level model as shown in Eq. (31). First, the periodic energy shift on $|2\rangle$ in the time domain can be converted to a series of modulation sidebands in the frequency domain through Jacobi-Anger expansion. In the rotating frame of $\frac{\delta}{2}\cos(2k_pv_jt + 2k_pz_{j,0})\sigma_{22}^j$, the Hamiltonian Eq. (31) becomes

$$H_j = \left(-\Delta_{12} + \frac{\delta}{2}\right)\sigma_{22}^j + \left[\frac{\Omega_{12,j}(t)}{2}e^{-i\frac{\delta\cdot\sin(2k_pv_jt+2k_pz_{j,0})}{4k_pv_j}}\sigma_{12}^j + h.c.\right]. \tag{32}$$

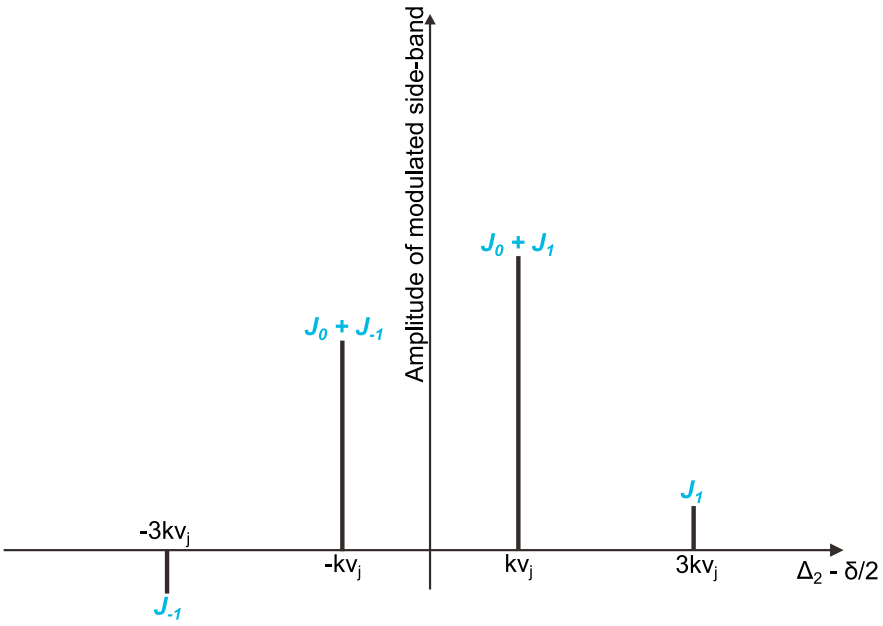

Supplemental Figure 7. Optical comb with a frequency difference of $2k_p v_j$ and sidebands of different amplitudes. Optical comb probes a static molecule that induces the same spectrum for a moving molecule in a standing-wave field.

According to the Jacobi-Anger expansion

$$e^{-i\zeta \sin\theta} = \sum_{n=-\infty}^{\infty} J_n(-\zeta) e^{in\theta}, \tag{33}$$

the Hamiltonian can be expanded as

$$H_j = \left(-\Delta_{12} + \frac{\delta}{2}\right)\sigma_{22}^j + \sum_{n=-\infty}^{\infty}\left[\frac{\Omega_{12,j}(t)}{2} J_n\left(-\zeta_j\right) e^{i2nk_p v_j t + i2nk_p z_{j,0}} \sigma_{12}^j + h.c.\right], \tag{34}$$

with $\zeta_j = \frac{\delta}{4k_p v_j}$. Substituting the moving induced time-dependent Rabi frequency

$$\Omega_{12,j}(t) = 2d_{12}\xi(e^{ik_p v_j t + ik_p z_{j,0}} + e^{-ik_p v_j t - ik_p z_{j,0}}), \tag{35}$$

which contributed a varying phase factor and was also related to the Doppler-effect, into Eq. (34), we obtain

$$\begin{aligned} H_j &= \left(-\Delta_{12} + \frac{\delta}{2}\right)\sigma_{22}^j + \left[\sum_{n=-\infty}^{\infty} d_{12}\xi J_n(-\zeta_j) e^{ik_p(2n+1)(v_j t + z_{j,0})}\sigma_{12}^j + \sum_{m=-\infty}^{\infty} d_{12}\xi J_n(-\zeta_j) e^{ik_p(2m-1)(v_j t + z_{j,0})}\sigma_{12}^j + h.c.\right] \\ &= \left(-\Delta_{12} + \frac{\delta}{2}\right)\sigma_{22}^j + \sum_{n=-\infty}^{\infty}\left[d_{12}\xi[J_n(-\zeta_j) + J_{n+1}(-\zeta_j)] e^{ik_p(2n+1)(v_j t + z_{j,0})}\sigma_{12}^j + h.c.\right]. \end{aligned} \tag{36}$$

Eventually, the time-dependent driving Hamiltonian for the moving molecules in a standing-wave probe field can be rewritten as a static molecule driven by multiple sidebands, i.e. a comb of drive lasers with a frequency difference of $2k_p v_j$. The amplitude of the comb tooth with the frequency of $2(n+1)k_p v_j (n \in Z)$ is contributed by the sum of $J_n(-\zeta_j) + J_{n+1}(-\zeta_j)$ as shown in Supplemental Fig. 7. To the first-order approximation for $|\zeta_j| \ll 1$, the two sidebands with amplitude of $J_{\pm 1}(-\zeta_j) \simeq \mp\frac{\zeta_j}{2}$ contribute to the probe with π phase difference and eventually lead to anti-symmetric absorption spectrum.

E. Analytic derivation of asymmetric spectral profile

1. Doppler-free Lamb-dip spectrum

In the following section, we further explain the asymmetric line-shape of the Lamb-dip spectrum through the asymptotic solution of the excitation probability $\mathcal{P}$. The $\mathcal{P}$ value can be determined by solving the density matrix via the master equation, however, it is extremely challenging to solve Eq. (36) with all sidebands involved. Most of the molecules contributing to the absorption spectrum, generally satisfy the limitation of $|\frac{\delta}{4k_pv_j}| \ll 1$. Hence we apply the approximation that only the two lowest-order sidebands are considered since $J_n(\zeta) \propto \zeta^n$. Therefore, the simplified Hamiltonian is

$$H_j = \left(-\Delta_{12} + \frac{\delta}{2}\right)\sigma_{22}^j + \frac{\Omega_{12,j}(t)}{2}\left[J_0\left(-\zeta_j\right) + J_1\left(-\zeta_j\right)e^{i2k_pv_jt+i2k_pz_{j,0}} + J_{-1}(-\zeta_j)e^{-i2k_pv_jt-i2k_pz_{j,0}}\right]\sigma_{12}^j + h.c. \quad (37)$$

For the Doppler-free Lamb-dip spectrum, similar to the treatments of the two-level limit, we can solve the system absorption in the limit of the closed system. The asymptotic Hamiltonian Eq. (37) can be rewritten as

$$\begin{aligned} H_j =& d_{12}\xi e^{-\frac{t^2}{2\tau^2}}\Big[J_0(-\zeta_j)(e^{-i(-\Delta_{12}+\frac{\delta}{2}-k_pv_j)t+ik_pz_{j,0}} + e^{-i(-\Delta_{12}+\frac{\delta}{2}+k_pv_j)t-ik_pz_{j,0}})+ \\ & J_1(-\zeta_j)(e^{-i(-\Delta_{12}+\frac{\delta}{2}-k_pv_j)t+ik_pz_{j,0}} - e^{-i(-\Delta_{12}+\frac{\delta}{2}+k_pv_j)t-ik_pz_{j,0}})\Big]\sigma_{12}^j + h.c. \end{aligned} \quad (38)$$

Thus, the interaction angle induced by the Rabi frequency of the probe field is

$$\begin{aligned} \theta_j(t) =& \int_{-\infty}^{\infty} \mathrm{d}t d_{12}\xi e^{-\frac{t^2}{2\tau^2}}\left[J_0(-\zeta_j)(e^{-i(-\Delta_{12}+\frac{\delta}{2}-k_pv_j)t+ik_pz_0} + e^{-i(-\Delta_{12}+\frac{\delta}{2}+k_pv_j)t-ik_pz_0})\right] \\ & + \int_{-\infty}^{\infty} \mathrm{d}t d_{12}\xi e^{-\frac{t^2}{2\tau^2}}\left[J_1(-\zeta_j)(e^{-i(-\Delta_{12}+\frac{\delta}{2}-k_pv_j)t+ik_pz_0} - e^{-i(-\Delta_{12}+\frac{\delta}{2}+k_pv_j)t-ik_pz_0})\right] \\ =& d_{12}\xi\sqrt{2\pi}\tau J_0(-\zeta_j)\left[e^{-\frac{1}{2}(-\Delta_{12}+\frac{\delta}{2}-k_pv_j)^2\tau^2+ik_pz_0} + e^{-\frac{1}{2}(-\Delta_{12}+\frac{\delta}{2}+k_pv_j)^2\tau^2-ik_pz_0}\right] \\ & + d_{12}\xi\sqrt{2\pi}\tau J_1(-\zeta_j)\left[e^{-\frac{1}{2}(-\Delta_{12}+\frac{\delta}{2}-k_pv_j)^2\tau^2+ik_pz_0} - e^{-\frac{1}{2}(-\Delta_{12}+\frac{\delta}{2}+k_pv_j)^2\tau^2-ik_pz_0}\right]. \end{aligned} \quad (39)$$

Since

$$\begin{aligned} \left|\theta_j^2(t)\right| =& \left(d_{12}\xi\sqrt{2\pi}\tau J_0(-\zeta_j)\right)^2\left(e^{-(-\Delta_{12}+\frac{\delta}{2}-k_pv_j)^2\tau^2} + e^{-(-\Delta_{12}+\frac{\delta}{2}+k_pv_j)^2\tau^2} + 2e^{-\left[\left(-\Delta_{12}+\frac{\delta}{2}\right)^2+(k_pv_j)^2\right]\tau^2}\cos\left(2k_pz_0\right)\right) \\ & + \left(d_{12}\xi\sqrt{2\pi}\tau J_1(-\zeta_j)\right)^2\left(e^{-(-\Delta_{12}+\frac{\delta}{2}-k_pv_j)^2\tau^2} + e^{-(-\Delta_{12}+\frac{\delta}{2}+k_pv_j)^2\tau^2} - 2e^{-\left[\left(-\Delta_{12}+\frac{\delta}{2}\right)^2+(k_pv_j)^2\right]\tau^2}\cos\left(2k_pz_0\right)\right) \\ & + \left(d_{12}\xi\sqrt{2\pi}\tau\right)^2 J_0(-\zeta_j)J_1(-\zeta_j)2\left(e^{-(-\Delta_{12}+\frac{\delta}{2}-k_pv_j)^2\tau^2} - e^{-(-\Delta_{12}+\frac{\delta}{2}+k_pv_j)^2\tau^2}\right), \end{aligned} \quad (40)$$

applying the relations Eq. (19) and Eq. (24), and noting that the difference between the two exponential function gives

$$\begin{aligned} & e^{-(-\Delta_{12}+\frac{\delta}{2}-k_pv_j)^2\tau^2} - e^{-(-\Delta_{12}+\frac{\delta}{2}+k_pv_j)^2\tau^2} \\ =& e^{-\Delta_{12}^2\tau^2-k_p^2v_j^2\tau^2}\left[e^{2\left(-\Delta_{12}+\frac{\delta}{2}\right)k_pv_j\tau^2} - e^{-2\left(-\Delta_{12}+\frac{\delta}{2}\right)k_pv_j\tau^2}\right] \\ \approx& e^{-\Delta_{12}^2\tau^2-k_p^2v_j^2\tau^2}\left[4\left(-\Delta_{12}+\frac{\delta}{2}\right)k_pv_j\tau^2\right], \end{aligned} \quad (41)$$

the absorption due to the second-order terms of θ_j is

$$\begin{aligned}
&\int_{-\infty}^{\infty} dv_j f(v_j) \int_0^{2\pi/k_p} \frac{dz_{j,0}}{2\pi/k_p} \left(\left|\theta_j^2(t)\right|\right) \\
&\approx \left(d_{12}\xi\sqrt{2\pi}\tau\right)^2 \frac{f(v_j=0)}{k_p} \left[J_0^2(-\zeta_j) 2\frac{\sqrt{\pi}}{\tau} + J_1^2(-\zeta_j) 2\frac{\sqrt{\pi}}{\tau} + 2J_0(-\zeta_j)J_1(-\zeta_j) e^{-\Delta_{12}^2\tau^2} \frac{\sqrt{\pi}}{\tau} 4\left(-\Delta_{12}+\frac{\delta}{2}\right) k_p v_j \tau^2\right].
\end{aligned} \tag{42}$$

Moreover, since $J_1(-\zeta_j) \ll J_0(-\zeta_j)$, we have

$$\begin{aligned}
&\int_{-\infty}^{\infty} dv_j f(v_j) \int_0^{2\pi/k_p} \frac{dz_{j,0}}{2\pi/k_p} \left(\left|\theta_j^2(t)\right|\right) \\
&\approx 4\pi^{3/2} \frac{f(v_j=0)}{k_p} J_0^2(-\zeta_j) \left(d_{12}\xi\right)^2 \tau + 16\pi^{3/2} \frac{f(v_j=0)}{k_p} J_0(-\zeta_j) J_1(-\zeta_j) k_p v_j \left(d_{12}\xi\right)^2 \tau^3 \left(-\Delta_{12}+\frac{\delta}{2}\right) e^{-\left(\Delta_{12}-\frac{\delta}{2}\right)^2\tau^2}.
\end{aligned} \tag{43}$$

It is surprising to find that the second term shows a spectral feature $\propto e^{-\left(\Delta_{12}-\frac{\delta}{2}\right)^2}$ around $\Delta_{12} \approx 0$, indicating a anti-symmetric absorption spectrum. Eventually, we solved the difference of the absorption spectrum to a background as

$$\begin{aligned}
\Delta\mathcal{P} &= 16\pi^{3/2} \frac{f(v_j=0)}{k_p} J_0(-\zeta_j) J_1(-\zeta_j) k_p v_j \left(d_{12}\xi\right)^2 \tau^3 \times (-\tilde{\Delta}_{12}) e^{-\tilde{\Delta}_{12}^2\tau^2} - \frac{8\sqrt{2}\pi^{5/2}}{3} \frac{f(v_j=0)}{k_p} J_0^4(-\zeta_j) \left(d_{12}\xi\right)^4 \tau^3 e^{-2\tilde{\Delta}_{12}^2\tau^2} \\
&\approx 16\pi^{3/2} \frac{f(v_j=0)}{k_p} J_1(-\zeta_j) k_p v_j \left(d_{12}\xi\right)^2 \tau^3 \times (-\tilde{\Delta}_{12}) e^{-\tilde{\Delta}_{12}^2\tau^2} - \frac{8\sqrt{2}\pi^{5/2}}{3} \frac{f(v_j=0)}{k_p} \left(d_{12}\xi\right)^4 \tau^3 e^{-2\tilde{\Delta}_{12}^2\tau^2} \\
&= -\frac{8\sqrt{2}\pi^{5/2}}{3} \frac{f(v_j=0)}{k_p} \left(d_{12}\xi\right)^4 \tau^3 \left[e^{-2\tilde{\Delta}_{12}^2\tau^2} - \frac{3\sqrt{2}}{8\pi} \frac{\delta}{\left(d_{12}\xi\right)^2} \times \tilde{\Delta}_{12} e^{-\tilde{\Delta}_{12}^2\tau^2}\right] \\
&= -\frac{8\sqrt{2}\pi^{5/2}}{3} \frac{f(v_j=0)}{k_p} \left(d_{12}\xi\right)^4 \tau^3 \left[e^{-2\tilde{\Delta}_{12}^2\tau^2} + \frac{3\sqrt{2}}{16\pi} \frac{\delta}{\left(d_{12}\xi\tau\right)^2} \times \frac{\partial e^{-\tilde{\Delta}_{12}^2\tau^2}}{\partial\tilde{\Delta}_{12}}\right]
\end{aligned} \tag{44}$$

where we take $J_{\pm1}(-\zeta_j) \simeq \mp\zeta_j/2$ for $|\zeta_j| \ll 1$, and $\tilde{\Delta}_{12} = \Delta_{12} - \delta/2$. Obviously, the asymmetry comes from the second term in Eq.(44). Moreover, $d_{12}\xi$ represents the Rabi frequency of the coupling between the weak transition and probe field, which can be replaced as

$$d_{12}\xi = \sqrt{\gamma_{12} \frac{3\lambda_{12}^3}{4\hbar\pi^2 c} \frac{I}{n}} \tag{45}$$

Here $\hbar$ is the Planck constant, c is the speed of light, n is the refractive index, and I is the intensity of the standing-wave laser field. Thus Eq.(44) can be rewritten as

$$\begin{aligned}
\Delta\mathcal{P} &= -\frac{8\sqrt{2}\pi^{5/2}}{3} \frac{f(v_j=0)}{k_p} \left(d_{12}\xi\right)^4 \tau^3 \left[e^{-2\tilde{\Delta}_{12}^2\tau^2} + \frac{3\sqrt{2}}{16\pi} \frac{\delta}{\left(d_{12}\xi\tau\right)^2} \times \frac{\partial e^{-\tilde{\Delta}_{12}^2\tau^2}}{\partial\tilde{\Delta}_{12}}\right] \\
&= -\frac{8\sqrt{2}\pi^{5/2}}{3} \frac{f(v_j=0)}{k_p} \left(d_{12}\xi\right)^4 \tau^3 \left[e^{-2\tilde{\Delta}_{12}^2\tau^2} + \frac{\sqrt{2}}{32\pi^2} \frac{\delta}{\gamma_{12}\tau^2} \frac{\hbar\omega_{12}^3}{c^2 I} \times \frac{\partial e^{-\tilde{\Delta}_{12}^2\tau^2}}{\partial\tilde{\Delta}_{12}}\right]
\end{aligned} \tag{46}$$

The analytical expression of $\Delta\mathcal{P}$ given in Eq.(46) further shows that the π phase difference of two sidebands $J_{\pm1}(-\frac{\delta}{4k_p v_j})$ leads to an anti-symmetric polarizability of the molecules, which contributes to the asymmetric absorption spectrum. Moreover, the dependence of the asymmetric degree on the modulation δ and decay rate γ_{12} are shown in Fig. 3(a) and 3(d) of the main text respectively, and we find that the numerical results agree well with Eq.(46).

2. Estimation of the Fano factor

To quantify the asymmetric degree of the calculated absorption spectra, the Doppler-free absorption profiles are fitted with the well-known Fano function

$$\mathcal{P} = A\frac{(q^2-1)}{1+(\frac{\omega_p-\omega_{12}+\omega_s}{\Gamma})^2} + 2Aq\frac{\frac{\omega_p-\omega_{12}+\omega_s}{\Gamma}}{1+(\frac{\omega_p-\omega_{12}+\omega_s}{\Gamma})^2} + B. \tag{47}$$

In the Fano function, the parameter A is the amplitude of the spectrum profile, B is the baseline amplitude, q shows the asymmetry degree, $\omega_p - \omega_{12} + \omega_s$ and Γ correspond to the frequency detuning and the width of the Fano profile respectively. Therefore, ω_s shows the frequency shift in the asymmetrical absorption spectrum.

The conventional Fano profile arises from the interference between two transition pathways, one towards a discrete excited state and the other to a continuum of states. In contrast, the asymmetry in this work is due to a nonlinear Fano-like resonance not with a continuum but with many distant discrete strong transitions. In addition, the Fano factor is limited to $|q| \leq 1$ for our mechanism.

By comparing our asymptotic expression of the Doppler-free absorption spectrum with the usual Fano function, we can find that the asymmetry is determined by the ratio between the symmetric term and the anti-symmetric term in Eq. (46). Therefore, we calculated the asymmetric degree as the ratio,

$$\tilde{q} \simeq \frac{\sqrt{2}\hbar\omega_{12}^3}{32\pi^2c^2}\frac{\delta\Delta_B}{\gamma_{12}I}. \tag{48}$$

Here $\Delta_B = 1/\tau$ is the transit-time broadening. We can find the dependence of the asymmetric degree $\tilde{q}$ shown in Eq. (48) with the parameters δ, γ_{12} and Δ_B, agrees well with our numerical calculated results shown in Fig. 3 in the main text, especially when $|q| \ll 1$. Considering the two factors from previous results: (1) the Fano factor q approximates the asymptotic results $\tilde{q}$ when $|q| \ll 1$; (2) $|q|$ should not exceed 1 since the asymmetry arises from the anti-symmetry of the Gaussian absorption spectrum, we made the conjecture of the Fano factor from the $\tilde{q}$ parameter as

$$q = \frac{\tilde{q}}{1+|\tilde{q}|}. \tag{49}$$

Then, we obtain $q \approx \tilde{q}$ for $|q|, |\tilde{q}| \ll 1$ and also $q \approx -1$ when $\tilde{q} \ll -1$ or $q \approx 1$ when $\tilde{q} \gg 1$. The equation is further numerically tested, as plotted by the blue line in Supplemental Fig. 11. More details are presented in Sec.(III B).

F. Theoretical discussion of the CO_2 experiments

Weak target lines (noted as $|2\rangle$ in our model) experimentally investigated in experiments of CO_2 are listed in Supplemental Table 1, from which we can calculate that $\lambda_{12} \simeq 1.6$ μm and $\omega_{12}/2\pi \simeq 1.9 \times 10^{14}$ Hz. Electronic transitions (noted as $|3\rangle$ in our model) of CO2 are located at approximately 108.85 nm with Einstein A-coefficients around $\mathcal{O}(10^9)$ s^{-1}[3]. Thus we can calculate that $\omega_{23}/2\pi \simeq 2.57 \times 10^{15}$ Hz, $\gamma_{23}/2\pi \simeq 1.59$ MHz, and $\Delta_{23}/2\pi \simeq 2.38 \times 10^{15}$ Hz. For CO_2 passing through a field with a waist width of $r = 0.5$ mm at room temperature (297 K), we estimate that the transit-time broadening is $\Delta_B/2\pi \simeq 0.11$ MHz. Provided that the Born-Oppenheimer approximation holds for the electronic states of CO_2, it is reasonable to assume that the electronic excited states are the same for all isotopologues. Thus the above parameters of electronic transitions can be applied to $^{13}CO_2$ and $^{12}CO_2$.

Similar to the example given in the main text following Eq.(1), when the modulation amplitude of δ is comparable with Δ_B (roughly $\delta \sim 0.1\Delta_B$), we can estimate that the NFR effect and the resulting asymmetric line profile can be observable. Thus substituting $\mathcal{P} \sim \mathcal{O}\left(10^{-4}\right)$, Δ_B, γ_{23} and Δ_{23} mentioned above into Eq. (1), we can estimate that the NFR effect can be observed when $\gamma_{12}/2\pi \lesssim 10^{-5}$ Hz. Compared with the experimental results shown in Fig. 4(c) in the main text, we find that the asymmetric line-shape almost disappears $q \sim 0$ for $\gamma_{12}/2\pi > 10^4$ Hz, which agrees well with our theoretical prediction.

We can estimate whether the asymmetry will appear in the spectrum not only according to Eq. (1) but also according to Eq. (4). According to Eq.(4), an asymmetric line be observed in case $\tilde{q}$ becomes significant ($\tilde{q} \gtrsim 0.1$). Moreover, we can see the influence of each parameter on the degree of asymmetry through Eq. (4), and even estimate a q value combination the rule of thumb $q = \tilde{q}/(1+\tilde{q})$. According to Eq.(4), obviously, the "benchmark of asymmetry $q = \tilde{q}/(1+\tilde{q})$" increases with δ/γ_{12} and Δ_B (the first term of $\tilde{q}$) but is irrelevant to intensity (the second term of $\tilde{q}$). For the specific estimated values of q, taking $\Delta_B/2\pi = 0.1$ MHz at room temperature for CO2, the q value of CO_2 is

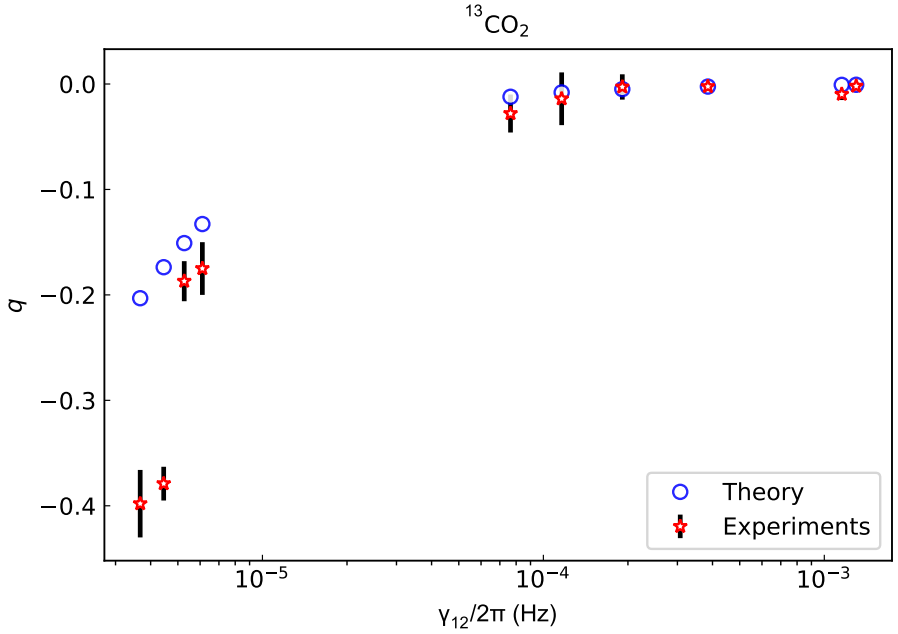

Supplemental Figure 8. Comparison between theoretical prediction results and experimental results. The theoretical results are obtained with Eq. (4) and the rule of thumb $q = \tilde{q}/(1+\tilde{q})$.

estimated as 0.203, 0.174, 0.151, 0.133, 0.012, 0.008, 0.005, 0.002, 0.001, and 0.001 for different experimental values of $\gamma_{12}/2\pi$ in Fig. 4(c), respectively. A more intuitive comparison can be found in Supplemental Figure 8. We find that the theoretical predictions basically match the experimental results except for the first two data points. For the difference of approximately 0.2 between the theoretical prediction and the experimental results for the first two data points, according to the comparison between the analytic and numerical results as shown in Supplemental Figure 11, we think it is within the reasonable range of error. With the parameters of Fig.4(d), $\gamma_{12}/2\pi = 1.6 \times 10^{-6}$ Hz, the q value independent of the light intensity is estimated to be -0.37. Comparing the estimated values of Figs. 4c & 4d with the experimental results, we find that they are basically consistent, which firmly supports our model.

III. NUMERICAL CALCULATION OF THE ABSORPTION SPECTRUM

To directly verify the mechanism of the proposed nonlinear Fano-like resonance and the dependence of the asymmetric degree on parameters, such as δ and γ_{12}, we numerically calculated the absorption to the long-lived energy level $|2\rangle$, which also corresponds to the probability $\mathcal{P}$ of the molecule excited to $|2\rangle$ when the molecule travels through the probe field. In the main text, the numerical results are presented in Figs. 2, 3, and 4. Here, we provide a detailed description of our numerical calculation method.

A. Method for Numerical calculation

For moving molecules at room temperature, the mean excitation probability $\mathcal{P}$ to the long-lived energy level $|2\rangle$ is calculated as

$$\mathcal{P} = \frac{i}{2}\int_{-\infty}^{\infty} f(v)dv \int_{0}^{\infty} g(v_t)dv_t \int_{0}^{\frac{r}{v_t}} [\Omega_{12}(v,t')\rho_{21}(v,t') - \Omega_{12}^{*}(v,t')\rho_{12}(v,t')]dt', \tag{50}$$

which averages over the ensemble of molecules by considering velocities along (v) and perpendicular (v_t) to the direction of the probe beam. The density matrix elements ρ_{12} and ρ_{21} can be acquired based on the Hamiltonian Eq.

(31) shown in Sec.(II C 2). We have

$$f(v) = \sqrt{\frac{m}{2\pi k_B T}} e^{-\frac{mv^2}{2k_B T}}, \tag{51}$$

and

$$g(v_t) = \frac{mv_t}{k_B T} e^{-\frac{mv_t^2}{2k_B T}}, \tag{52}$$

which are the one-dimensional and two-dimensional Maxwell-Boltzmann distribution functions, respectively. Here, m denotes the mass of a single molecule, k_B is the Boltzmann constant, and T is the temperature. For a beam waist width of r, the transit time of the molecule is $\tau = \frac{r}{v_t}$, and the temporal integration relies on the fact that the position of molecules is uniformly distributed in the beam, which equivalently gives a uniform distribution of instances in the time domain. The density matrix element $\rho_{12}(t)$ can be obtained numerically by solving the differential equations of density matrix elements based on the Hamiltonian and master equation, as described in the previous section. The integrals are numerically implemented by discretizing the velocities and time into steps, i.e. continuous integrals are replaced by discrete sums as

$$\mathcal{P} = \frac{i}{2} \sum_{v=-\infty}^{\infty} f(v)dv \sum_{v_t=0}^{\infty} g(v_t)dv_t \sum_{t'=0}^{\frac{r}{v_t}} [\Omega_{12}(v,t^{'})\rho_{21}(v,t^{'}) - \Omega_{12}^{*}(v,t^{'})\rho_{12}(v,t^{'})]dt^{'} \tag{53}$$

Supplemental Fig. 9 explains the details of the numerical simulations. Shown in Supplemental Fig. 9(a) is the excitation probability versus the probe frequency detuning $\Delta_{12} = \omega_p - \omega_{12}$ for molecules at a given longitudinal velocity v and a given transit time τ. Due to the Doppler effect, the $\mathcal{P}$ is nonzero when the probe laser matches the velocity of the molecule, and the spectrum shows a broadening due to the transit time. For a given v, when averaging over the distribution of v_t, i.e. the τ, the spectrum shows a smoother broadening, as shown in Supplemental Fig. 9(b). If τ is fixed and taking average over v, we observe a full absorption spectrum, showing dips at the center $\Delta_{12} \approx 0$ due to the saturation absorption effect. However, for different τ, the spectrum shows different asymmetric spectral profiles. When solving the full model by averages over all three variables, we arrive at the final spectrum. Shown in Supplemental Fig. 9(d) is a typical spectrum, with a fitting Fano factor of -0.35.

Absorption spectra for a single molecule with different modulation amplitudes δ are calculated with the ensemble average of longitudinal speed $\langle v \rangle$ and transit time $\langle \tau \rangle$, and the results are shown in Supplemental Fig. 10. In Supplemental Fig. 10(a)-(c), we can find that the asymmetric degree, which is quantified by the Fano factor q, increases with $|\delta|$, and the dependence of the asymmetric degree on the modulation amplitude is also shown in Fig. 3(a) in the main text. For the numerical calculation in the main text, we only considered the situation that the AC Stark shifts on $|2\rangle$ is larger than that on $|1\rangle$, thus $\delta < 0$ is taken in our numerical calculation. However, situation that $\delta > 0$ is also possible, which relates to the transition dipole moments. Absorption spectra for a single molecule with $\delta > 0$ are shown in Supplemental Figs. 10(a)-(c). We can find that the same modulation amplitude $|\delta|$ leads to the same asymmetric degree and the sign of δ determines the sign of asymmetric degree q. In the Doppler-free absorption spectrum, the asymmetric degree depends on not only the modulation amplitude δ, but also the decay rate γ_{12} and the transit-time broadening, which has been systematically studied in the main text. Further discussions about the dependence on parameters are provided in the next section.

B. Comparison of the analytic results of the Fano factor(q) with the numerical results

We can acquire the dependence of the asymmetric degree on the parameters δ, γ_{12} and Δ_B, according to Eq. (48) and (49). Here, the relation between the asymmetric degree and δ/γ_{12} is further investigated, and the numerical results are summarized in Supplemental Fig. 11. The results are also shown in Fig. 3(e) in the main text and we can find that the asymmetric degree q increases when δ increases and γ_{12} decreases. From the projection of Fig. 3(e) in the main text, the contour lines with the asymmetric degree q are approximately coincident with the yellow lines, which are plotted by setting δ/γ_{12} constant. The numerically fitted q shows a typical saturation-like behavior when increasing the dimensionless parameter δ/γ_{12}, thus we fit the curve by an empirical saturation formula

$$q = \frac{\delta/\gamma_{12}}{10^{9.4} + |\delta/\gamma_{12}|}. \tag{54}$$

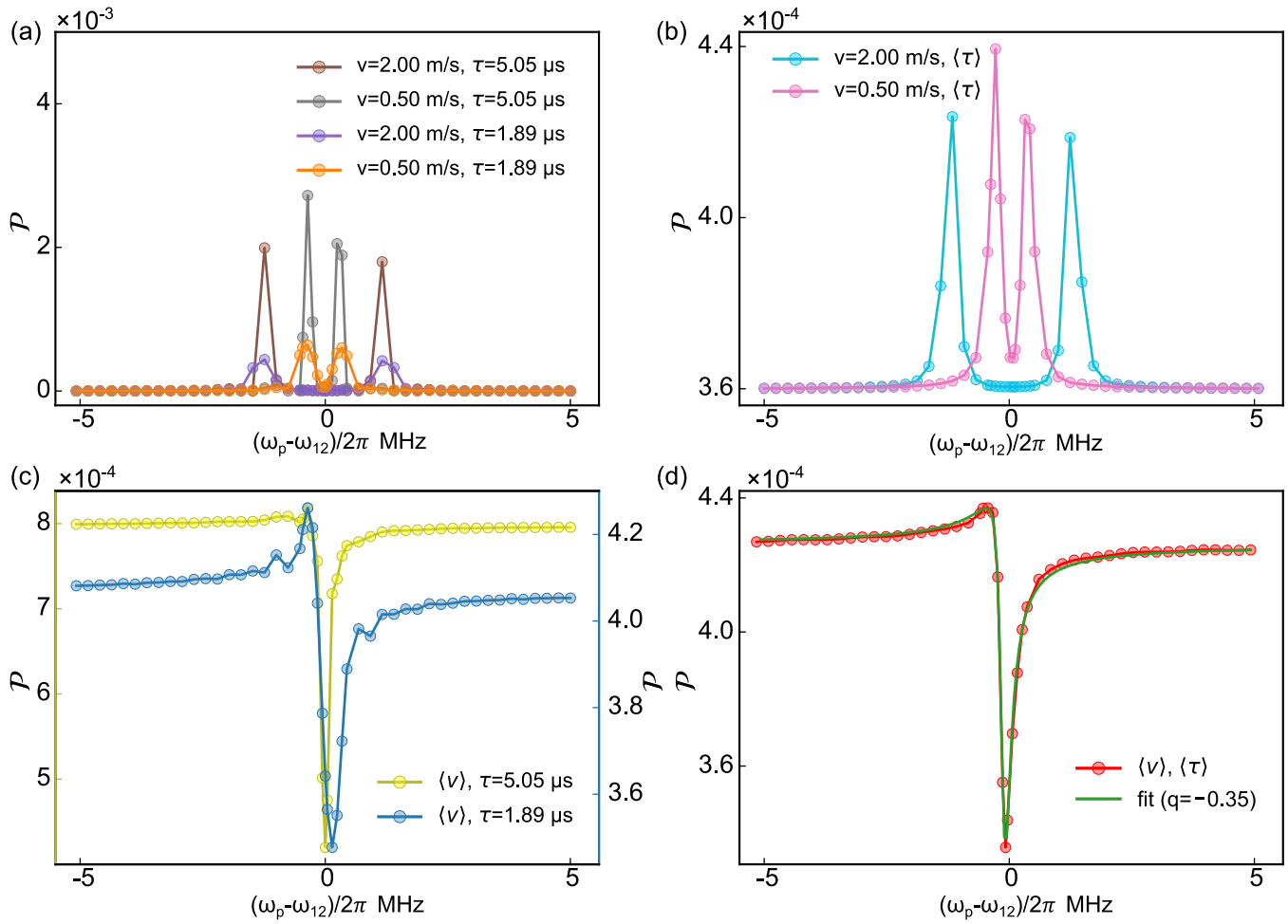

Supplemental Figure 9. Numerically solved absorption spectra. (a) The spectrum for a given longitudinal velocity v and transit time τ. (b) The spectrum for a given v, but average over the ensemble with different transit time τ. (c) The spectrum for a given transit time τ, but average over the ensemble with different longitudinal speed. (d) A typical spectrum by the full model corresponding to an ensemble average of all three integrals. In the main text, all the numerical results are implemented with the full model. Moreover, to further verify the proposed model, we take another set of parameters that $\Omega_{12}/2\pi$=0.07 MHz, $\gamma_{12}/2\pi = 0.4 \times 10^{-11}$ MHz, $\delta/2\pi = -0.07$ MHz, the relative molecular mass is 45, the temperature is 295 K and the beam waist width of the standing-wave field is 0.5 mm.

As shown by the red line in Supplemental Fig. 11, with the black circles representing the data points, the empirical formula fits the numerical results very well. When $\delta/\gamma_{12} \sim \mathcal{O}(10^{9.4})$, asymmetry can be shown in the absorption spectrum and the asymmetric degree q increases with increasing δ and decreasing γ_{12}. Thus we can estimate the asymmetric degree q with given δ and γ_{12} to estimate the influence of excess transitions in far-off resonance without complex numerical calculations. Moreover, the blue line calculated with the empirical formula [Eq. (48) and (49)] is slightly underneath the numerical results, which implies that the estimated asymmetric degree q with Eq. (48) and (49) are smaller than the real asymmetric degree. This is because we have ignored the terms of high-order sidebands $(J_n(-\zeta_j), n \geq 2)$, which also contribute to the asymmetry of the spectrum. Without any fitting parameter, the excellent agreement between the conjectured formula and numerical results confirms our physical mechanism and asymptotic derivations, and also provides an experimentally feasible criterion for evaluating the asymmetric spectral profile of the proposed nonlinear Fano-like resonance.

C. Simulation for hydrogen deuteride(HD)

In this section, we show detailed information for the calculations about the asymmetric Doppler-free absorption profile of HD, to support that the proposed mechanism can be used to explain the asymmetric profile observed in

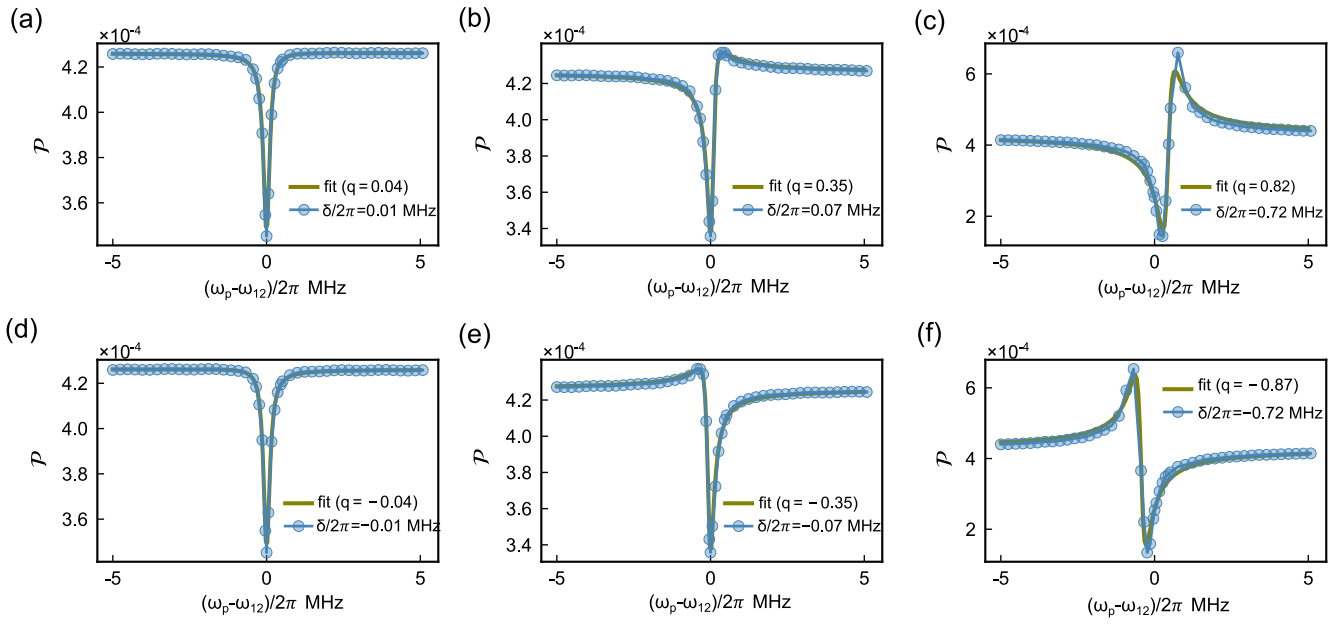

Supplemental Figure 10. Asymmetric Doppler-free absorption spectra for different δ. (a)-(f) The spectra of the mean excitation probability of a single molecule $\mathcal{P}$ for different modulation amplitude δ. Other parameters are the same as those in Supplementar Fig. 9.

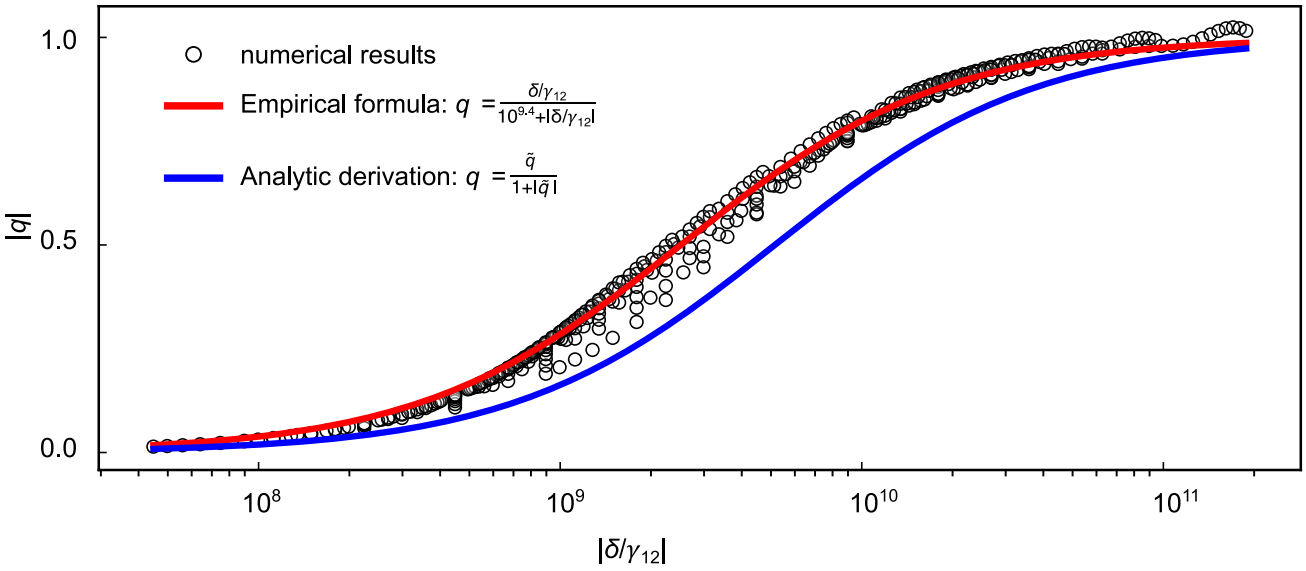

Supplemental Figure 11. The dependence of the Fano factor on the dimensionless parameter δ/γ_{12}. Circles are the Fano factors q, which are acquired by fitting the numerically solved absorption spectra with the Fano function, and the same numerical results are also shown in Fig. 3(e) in the main text. The red line is the fitting curve by the empirical saturation formula $q = \delta/\gamma_{12}/(10^{9.4} + |\delta/\gamma_{12}|)$. The blue line shows the calculation of the expected Fano factor by the conjecture formula $q = \tilde{q}/(1 + |\tilde{q}|)$ [Eq. (49)] without any fitting parameter.

the cavity-enhanced saturated absorption spectroscopy of HD [7, 8]. We choose the parameters according to the experiments, in which the R(1) transition of HD [9, 10] ($|1\rangle \rightarrow |2\rangle$) is the target transition to be measured, as shown in Supplementarl Fig. 12(a)). In the experiments, the transition width is $\gamma_{12}/2\pi = 3.4 \times 10^{-6}$ Hz, and the transition is probed by a standing-wave field of wavelength $\lambda \approx 1380$ nm, and we choose a beam waist width of 0.5 mm and an intracavity power of 210 W. To account for the potential far-off-resonance that induces the nonlinear Fano effect, we introduce a distant electronic state denoted $|3\rangle$ with a spontaneous emission rate of $\gamma_{13}/2\pi = \gamma_{23}/2\pi = 280$ MHz to

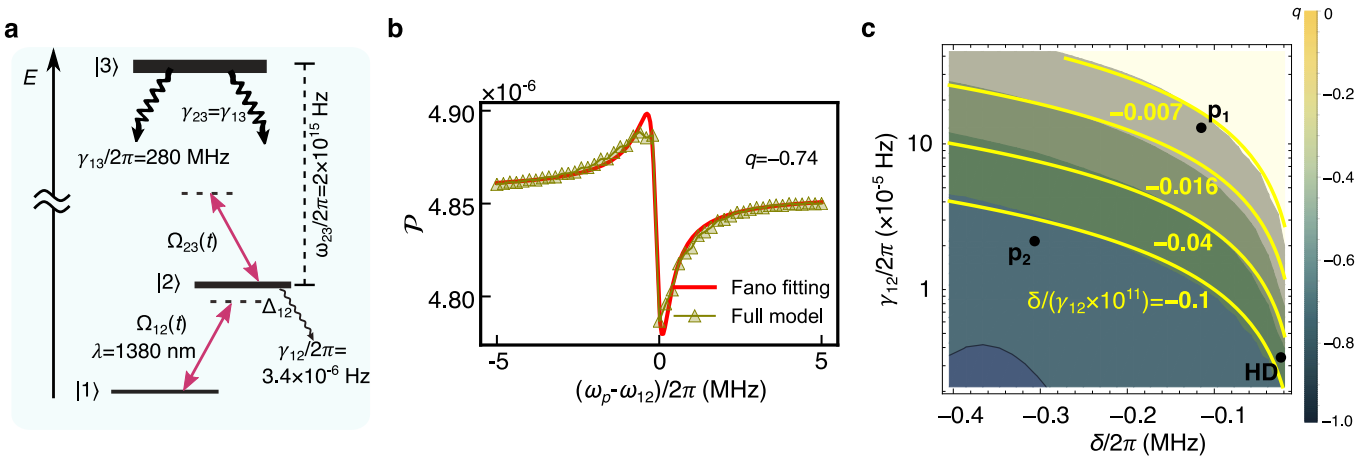

Supplemental Figure 12. Energy level structure and simulation results for HD. (a) Energy structure for relevant energy levels of HD. The parameters are: $\gamma_{13}/2\pi = \gamma_{23}/2\pi = 280$ MHz, $\gamma_{12}/2\pi = 3.4 \times 10^{-6}$ Hz. (b) Simulated Doppler-free absorption spectrum for HD with an intracavity standing-wave power of 210 W and a beam waist width of 0.5 mm. (c) Projection of Fig. 3(e) in the main text.

$|1(2)\rangle$, which is selected according to [9, 10]. Note that there might be other relevant energy levels that contribute to the nonlinear Fano effect in experiments, we select only the electronic transition that is mostly close to the target transition. In this model, the probe field couples with the narrow transition on resonance with Rabi frequency $\Omega_{12}/2\pi = 0.03$ MHz, and simultaneously far off-resonantly couples with the electric state transition ($|1\rangle \rightarrow |3\rangle$ and $|2\rangle \rightarrow |3\rangle$) (see Supplementarl Fig. 12(a)), with Rabi frequency of $\Omega_{13}/2\pi = 9143$ MHz, $\Omega_{23}/2\pi = 10672$ MHz and detuning of $\Delta_{13}/2\pi = -2.0 \times 10^{15}$ Hz, $\Delta_{23}/2\pi = -1.8 \times 10^{15}$ Hz, respectively. Thus the effective modulation amplitude on $|2\rangle$ from the two far off-resonant couplings is calculated as

$$\delta/2\pi = \left(\frac{\Omega_{23}^2}{\Delta_{23}} - \frac{\Omega_{12}^2}{\Delta_{12}}\right)/2\pi = -0.022 \text{ MHz}. \tag{55}$$

Note that the AC Stark shift on the ground and excited states have opposite sign. By the full-model simulation of the Floquet Hamiltonian of the modulating molecules, the Doppler-free absorption spectrum of the R(1) transition in HD is simulated with the above parameters and the result is shown in Supplemental Fig. 12(b). Moreover, the parameter of the R(1) transition in HD is involved in the three-dimensional image shown in Fig. 3(e) of the main text and can also be directly shown in Supplemental Fig. 12(c). In conclusion, the proposed nonlinear Fano-like resonance can induce asymmetric Doppler-free absorption spectra of HD with a simulated Fano factor $|q| > 0.05$, which agrees with the observed spectra in experiments [7, 8, 11, 12]. Thus, the proposed mechanism could explain the puzzling profile observed in the cavity-enhanced absorption spectroscopy of HD [7, 8, 11, 12].

D. Frequency shift due to NFR for CO_2

As we mentioned in the main text, the proposed mechanism of NFR will induce a systematic error of line center for the spectral measurement of narrow transitions. In our numerical calculation, the fitting parameter ω_s implies the fitting frequency shift with respect to the influence of the mechanism of NFR, thus we can use the fitted frequency shift ω_s to estimate the systematic error induced by NFR. For the simulation of CO_2, the fitted frequency shift ω_s with $\delta/2\pi$ of -0.07 ± 0.02 MHz is shown in Supplemental Fig. 13. Considering that the accurate position of the line center relates to the line profile, we only estimate systematic errors of line center introduced by the proposed NFR model instead of an accurate line center. Therefore the frequency shifts ω_s for these lines are not given in the main text. From Supplemental Fig. 13(a), we can find that ω_s oscillates up and down with the change of γ_{12} when the light intensity is fixed. The dependence between the fitting center ω_s and γ_{12} requires further study. When γ_{12} is fixed, ω_s increases with the standing wave field intensity I as shown in Supplemental Fig. 13(b), which is consistent with our numerical calculation of Fig. 3(a) in the main text. The result could be well understood, because an enhanced light intensity leads to a higher modulation amplitude, which in turn leads to a greater central frequency shift.

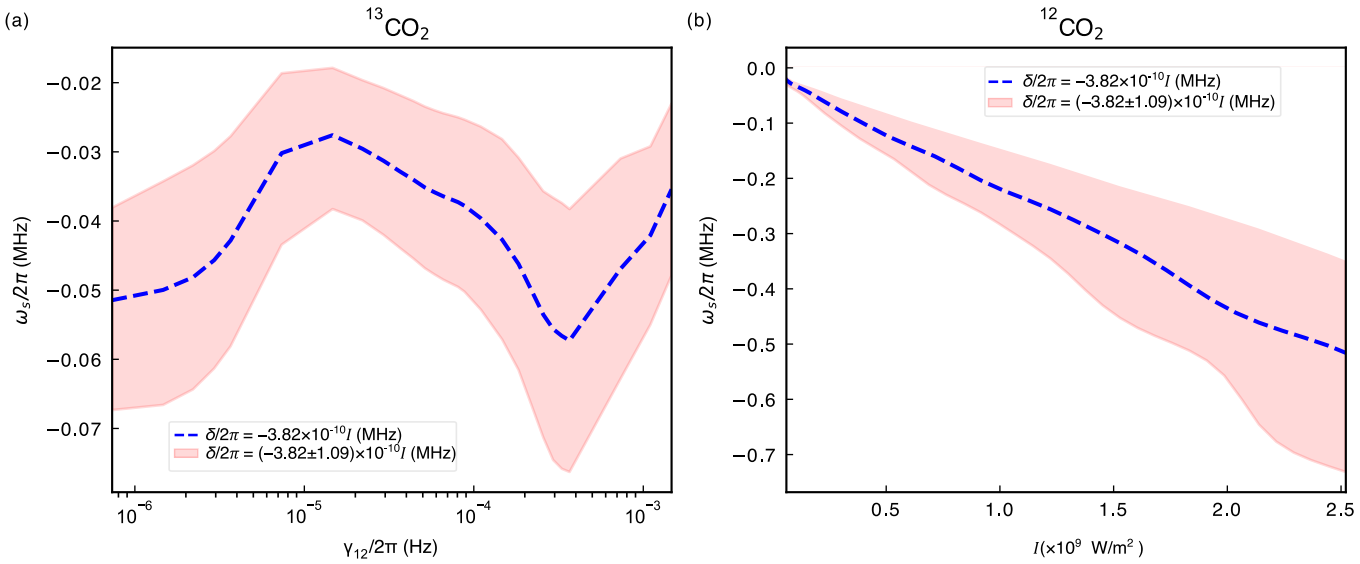

Supplemental Figure 13. (a) Dependence of $\omega_s/2\pi$ on $\gamma_{12}/2\pi$ of $^{13}CO_2$ with a standing-wave field intensity of $I = 1.83 \times 10^8$ W/m^2. c(b) Dependence of $\omega_s/2\pi$ on the standing-wave field intensity I of $^{12}CO_2$ with $\gamma_{12}/2\pi = 1.63 \times 10^{-6}$ Hz.

[1] I. E. Gordon, L. Rothman, C. Hill, R. Kochanov, Y. Tan, P. F. Bernath, M. Birk, V. Boudon, A. Campargue, K. Chance, B. Drouin, J.-M. Flaud, R. Gamache, J. Hodges, D. Jacquemart, V. Perevalov, A. Perrin, K. Shine, M.-A. Smith, J. Tennyson, G. Toon, H. Tran, V. Tyuterev, A. Barbe, A. Császár, V. Devi, T. Furtenbacher, J. Harrison, J.-M. Hartmann, A. Jolly, T. Johnson, T. Karman, I. Kleiner, A. Kyuberis, J. Loos, O. Lyulin, S. Massie, S. Mikhailenko, N. Moazzen-Ahmadi, H. Müller, O. Naumenko, A. Nikitin, O. Polyansky, M. Rey, M. Rotger, S. Sharpe, K. Sung, E. Starikova, S. Tashkun, J. V. Auwera, G. Wagner, J. Wilzewski, P. Wcisło, S. Yu, and E. Zak, J. Quant. Spectrosc. Radiat. Transf. **203**, 3 (2017).

[2] H.-P. Breuer and F. Petruccione, The Theory of Open Quantum Systems (Oxford University Press, Oxford, England, UK, 2002) p. 122.

[3] H. Keller-Rudek, G. K. Moortgat, R. Sander, and R. Sörensen, Earth Syst. Sci. Data **5**, 365 (2013).

[4] Z. Lu, Y. C. Chang, Y. Benitez, Z. Luo, A. B. Houria, T. Ayari, M. M. Al Mogren, M. Hochlaf, W. M. Jackson, and C. Y. Ng, Phys. Chem. Chem. Phys. **17**, 11752 (2015).

[5] J. Zhou, Z. Luo, J. Yang, Y. Chang, Z. Zhang, Y. Yu, Q. Li, G. Cheng, Z. Chen, Z. He, L. Che, S. Yu, G. Wu, K. Yuan, and X. Yang, Phys. Chem. Chem. Phys. **22**, 6260 (2020).

[6] S. Yu. Grebenshchikov, J. Chem. Phys. **138**, 224107 (2013).

[7] L.-G. Tao, A.-W. Liu, K. Pachucki, J. Komasa, Y. R. Sun, J. Wang, and S.-M. Hu, Phys. Rev. Lett. **120**, 153001 (2018).

[8] F. M. J. Cozijn, P. Dupré, E. J. Salumbides, K. S. E. Eikema, and W. Ubachs, Phys. Rev. Lett. **120**, 153002 (2018).

[9] H. Abgrall and E. Roueff, Astronomy & Astrophysics **445**, 361 (2006).

[10] U. Fantz and D. Wünderlich, At. Data Nucl. Data Tables **92**, 853 (2006).

[11] M. L. Diouf, F. M. J. Cozijn, B. Darquié, E. J. Salumbides, and W. Ubachs, Opt. Lett. **44**, 4733 (2019).

[12] T. P. Hua, Y. R. Sun, J. Wang, C. L. Hu, L. G. Tao, A. W. Liu, and S. M. Hu, Chinese J. Chem. Phys. **32**, 107 (2019).